


Measurement of $D^{*}(+/-)$ meson production and determination of $F_2(c\bar{c})$ at low Q^2 in deep-inelastic scattering at HERA

Journal Article**Author(s):**

H1 Collaboration; Aaron, Francise D.; [Grab, Christophorus](#) ; et al.

Publication date:

2011-10

Permanent link:

<https://doi.org/10.3929/ethz-b-000041093>

Rights / license:

[Creative Commons Attribution 4.0 International](#)

Originally published in:

The European Physical Journal C 71(10), <https://doi.org/10.1140/epjc/s10052-011-1769-0>

Measurement of $D^{*\pm}$ meson production and determination of F_2^{cc} at low Q^2 in deep-inelastic scattering at HERA

The H1 Collaboration

F.D. Aaron^{5,h}, C. Alexa⁵, V. Andreev²⁵, S. Backovic³⁰, A. Baghdasaryan³⁸, S. Baghdasaryan³⁸, E. Barrelet²⁹, W. Bartel¹¹, K. Begzsuren³⁵, A. Belousov²⁵, P. Belov¹¹, J.C. Bizot²⁷, M.-O. Boenig⁸, V. Boudry²⁸, I. Bozovic-Jelisavcic², J. Bracinik³, G. Brandt¹¹, M. Brinkmann¹¹, V. Brisson²⁷, D. Britzger¹¹, D. Bruncko¹⁶, A. Bunyatyan^{13,38}, G. Buschhorn^{26,†}, L. Bystritskaya²⁴, A.J. Campbell¹¹, K.B. Cantun Avila²², F. Ceccopieri⁴, K. Cerny³², V. Cerny^{16,g}, V. Chekelian²⁶, J.G. Contreras²², J.A. Coughlan⁶, J. Cvach³¹, J.B. Dainton¹⁸, K. Daum^{37,c}, B. Delcourt²⁷, J. Delvax⁴, E.A. De Wolf⁴, C. Diaconu²¹, M. Dobre^{12,j,k}, V. Dodonov¹³, A. Dossanov²⁶, A. Dubak^{30,f}, G. Eckerlin¹¹, S. Egl³⁶, A. Eliseev²⁵, E. Elsen¹¹, L. Favart⁴, A. Fedotov²⁴, R. Felst¹¹, J. Feltesse¹⁰, J. Ferencei¹⁶, D.-J. Fischer¹¹, M. Fleischer¹¹, A. Fomenko²⁵, E. Gabathuler¹⁸, J. Gayler¹¹, S. Ghazaryan¹¹, A. Glazov¹¹, L. Goerlich⁷, N. Gogitidze²⁵, M. Gouzevitch^{11,e}, C. Grab⁴⁰, A. Grebenyuk¹¹, T. Greenshaw¹⁸, B.R. Grell¹¹, G. Grindhammer²⁶, S. Habib¹¹, D. Haidt¹¹, C. Helebrant¹¹, R.C.W. Henderson¹⁷, E. Hennekemper¹⁵, H. Henschel³⁹, M. Herbst¹⁵, G. Herrera²³, M. Hildebrandt³⁶, K.H. Hiller³⁹, D. Hoffmann²¹, R. Horisberger³⁶, T. Hreus^{4,d}, F. Huber¹⁴, M. Jacquet²⁷, X. Janssen⁴, L. Jönsson²⁰, A.W. Jung¹⁵, H. Jung^{11,4,1}, M. Kapichine⁹, I.R. Kenyon³, C. Kiesling²⁶, M. Klein¹⁸, C. Kleinwort¹¹, T. Kluge¹⁸, R. Kogler¹¹, P. Kostka³⁹, M. Kraemer¹¹, J. Kretzschmar¹⁸, K. Krüger^{15,a}, M.P.J. Landon¹⁹, W. Lange³⁹, G. Laštovička-Medin³⁰, P. Laycock¹⁸, A. Lebedev²⁵, V. Lendermann¹⁵, S. Levonian¹¹, K. Lipka^{11,j}, B. List¹², J. List¹¹, R. Lopez-Fernandez²³, V. Lubimov²⁴, A. Makankine⁹, E. Malinowski²⁵, P. Marage⁴, H.-U. Martyn¹, S.J. Maxfield¹⁸, A. Mehta¹⁸, A.B. Meyer¹¹, H. Meyer³⁷, J. Meyer¹¹, S. Mikocki⁷, I. Milcewicz-Mika⁷, F. Moreau²⁸, A. Morozov⁹, J.V. Morris⁶, M. Mudrinic², K. Müller⁴¹, Th. Naumann³⁹, P.R. Newman³, C. Niebuhr¹¹, D. Nikitin⁹, G. Nowak⁷, K. Nowak¹¹, J.E. Olsson¹¹, D. Ozerov²⁴, P. Pahl¹¹, V. Palichik⁹, I. Panagoulas^{11,b,x}, M. Pandurovic², Th. Papadopoulou^{11,b,x}, C. Pascaud²⁷, G.D. Patel¹⁸, E. Perez^{10,e}, A. Petrukhin¹¹, I. Picuric³⁰, S. Piec¹¹, H. Pirumov¹⁴, D. Pitzl¹¹, R. Plačakytė¹², B. Pokorny³², R. Polifka³², B. Povh¹³, V. Radescu¹⁴, N. Raicevic³⁰, T. Ravdandorj³⁵, P. Reimer³¹, E. Rizvi¹⁹, P. Robmann⁴¹, R. Roosen⁴, A. Rostovtsev²⁴, M. Rotaru⁵, J.E. Ruiz Tabasco²², S. Rusakov²⁵, D. Šálek³², D.P.C. Sankey⁶, M. Sauter¹⁴, E. Sauvan²¹, S. Schmitt¹¹, L. Schoeffel¹⁰, A. Schöning¹⁴, H.-C. Schultz-Coulon¹⁵, F. Sefkow¹¹, L.N. Shtarkov²⁵, S. Shushkevich²⁶, T. Sloan¹⁷, I. Smiljanic², Y. Soloviev²⁵, P. Sopicki⁷, D. South¹¹, V. Spaskov⁹, A. Specka²⁸, Z. Staykova¹¹, M. Steder¹¹, B. Stella³³, G. Stoicea⁵, U. Straumann⁴¹, T. Sykora^{4,32}, P.D. Thompson³, T. Toll¹¹, T.H. Tran²⁷, D. Traynor¹⁹, P. Truöl⁴¹, I. Tsakov³⁴, B. Tseepeldorj^{35,i}, J. Turnau⁷, K. Urban¹⁵, A. Valkárová³², C. Vallée²¹, P. Van Mechelen⁴, Y. Vazdik²⁵, D. Wegener⁸, E. Wünsch¹¹, J. Žáček³², J. Zálešák³¹, Z. Zhang²⁷, A. Zhokin²⁴, H. Zohrabyan³⁸, F. Zomer²⁷

¹I. Physikalisches Institut der RWTH, Aachen, Germany

²Vinca Institute of Nuclear Sciences, University of Belgrade, 1100 Belgrade, Serbia

³School of Physics and Astronomy, University of Birmingham, Birmingham, UKⁿ

⁴Inter-University Institute for High Energies ULB-VUB, Brussels and Universiteit Antwerpen, Antwerpen, Belgium^o

⁵National Institute for Physics and Nuclear Engineering (NIPNE), Bucharest, Romania^y

⁶Rutherford Appleton Laboratory, Chilton, Didcot, UKⁿ

⁷Institute for Nuclear Physics, Cracow, Poland^p

⁸Institut für Physik, TU Dortmund, Dortmund, Germany^m

⁹Joint Institute for Nuclear Research, Dubna, Russia

¹⁰CEA, DSM/Irfu, CE-Saclay, Gif-sur-Yvette, France

¹¹DESY, Hamburg, Germany

¹²Institut für Experimentalphysik, Universität Hamburg, Hamburg, Germany^m

¹³Max-Planck-Institut für Kernphysik, Heidelberg, Germany

¹⁴Physikalisches Institut, Universität Heidelberg, Heidelberg, Germany^m

¹⁵Kirchhoff-Institut für Physik, Universität Heidelberg, Heidelberg, Germany^m

¹⁶Institute of Experimental Physics, Slovak Academy of Sciences, Košice, Slovak Republic^r

¹⁷Department of Physics, University of Lancaster, Lancaster, UKⁿ

¹⁸Department of Physics, University of Liverpool, Liverpool, UKⁿ

- ¹⁹Queen Mary and Westfield College, London, UK^a
²⁰Physics Department, University of Lund, Lund, Sweden^b
²¹CPPM, Aix-Marseille Université, CNRS/IN2P3, 13288 Marseille, France
²²Departamento de Física Aplicada, CINVESTAV, Mérida, Yucatán, México^v
²³Departamento de Física, CINVESTAV IPN, México City, México^v
²⁴Institute for Theoretical and Experimental Physics, Moscow, Russia^w
²⁵Lebedev Physical Institute, Moscow, Russia^q
²⁶Max-Planck-Institut für Physik, München, Germany
²⁷LAL, Université Paris-Sud, CNRS/IN2P3, Orsay, France
²⁸LLR, Ecole Polytechnique, CNRS/IN2P3, Palaiseau, France
²⁹LPNHE, Université Pierre et Marie Curie Paris 6, Université Denis Diderot Paris 7, CNRS/IN2P3, Paris, France
³⁰Faculty of Science, University of Montenegro, Podgorica, Montenegro^z
³¹Institute of Physics, Academy of Sciences of the Czech Republic, Praha, Czech Republic^t
³²Faculty of Mathematics and Physics, Charles University, Praha, Czech Republic^t
³³Dipartimento di Fisica Università di Roma Tre and INFN Roma 3, Roma, Italy
³⁴Institute for Nuclear Research and Nuclear Energy, Sofia, Bulgaria^q
³⁵Institute of Physics and Technology of the Mongolian Academy of Sciences, Ulaanbaatar, Mongolia
³⁶Paul Scherrer Institut, Villigen, Switzerland
³⁷Fachbereich C, Universität Wuppertal, Wuppertal, Germany
³⁸Yerevan Physics Institute, Yerevan, Armenia
³⁹DESY, Zeuthen, Germany
⁴⁰Institut für Teilchenphysik, ETH, Zürich, Switzerland^u
⁴¹Physik-Institut der Universität Zürich, Zürich, Switzerland^u

Received: 6 June 2011 / Revised: 31 August 2011 / Published online: 12 October 2011
 © The Author(s) 2011. This article is published with open access at Springerlink.com

Abstract Inclusive production of D^* mesons in deep-inelastic ep scattering at HERA is studied in the range $5 < Q^2 < 100 \text{ GeV}^2$ of the photon virtuality and $0.02 < y < 0.7$ of the inelasticity of the scattering process. The observed phase space for the D^* meson is $p_T(D^*) > 1.25 \text{ GeV}$ and $|\eta(D^*)| < 1.8$. The data sample corresponds to an integrated luminosity of 348 pb^{-1} collected with the H1 detector. Sin-

gle and double differential cross sections are measured and the charm contribution $F_2^{c\bar{c}}$ to the proton structure function F_2 is determined. The results are compared to perturbative QCD predictions at next-to-leading order implementing different schemes for the charm mass treatment and with Monte Carlo models based on leading order matrix elements with parton showers.

^ae-mail: kruegerk@mail.desy.de

^bAlso at Physics Department, National Technical University, Zografou Campus, GR-15773 Athens, Greece.

^cAlso at Rechenzentrum, Universität Wuppertal, Wuppertal, Germany.

^dAlso at University of P.J. Šafárik, Košice, Slovak Republic.

^eAlso at CERN, Geneva, Switzerland.

^fAlso at Max-Planck-Institut für Physik, München, Germany.

^gAlso at Comenius University, Bratislava, Slovak Republic.

^hAlso at Faculty of Physics, University of Bucharest, Bucharest, Romania.

ⁱAlso at Ulaanbaatar University, Ulaanbaatar, Mongolia.

^jSupported by the Initiative and Networking Fund of the Helmholtz Association (HGF) under the contract VH-NG-401.

^kAbsent on leave from NIPNE-HH, Bucharest, Romania.

^lOn leave of absence at CERN, Geneva, Switzerland.

^mSupported by the Bundesministerium für Bildung und Forschung, FRG, under contract numbers 05H09GUF, 05H09VHC, 05H09VHF, 05H16PEA.

ⁿSupported by the UK Science and Technology Facilities Council, and formerly by the UK Particle Physics and Astronomy Research Council.

^oSupported by FNRS-FWO-Vlaanderen, IISN-IKW and IWT and by Interuniversity Attraction Poles Programme, Belgian Science Policy.

^pPartially Supported by Polish Ministry of Science and Higher Education, grant DPN/N168/DESY/2009.

^qSupported by the Deutsche Forschungsgemeinschaft.

^rSupported by VEGA SR grant no. 2/7062/ 27.

^sSupported by the Swedish Natural Science Research Council.

^tSupported by the Ministry of Education of the Czech Republic under the projects LC527, INGO-LA09042 and MSM0021620859.

^uSupported by the Swiss National Science Foundation.

^vSupported by CONACYT, México, grant 48778-F.

^wRussian Foundation for Basic Research (RFBR), grant no. 1329.2008.2 and Rosatom.

^xThis project is co-funded by the European Social Fund (75%) and National Resources (25%) - (EPEAEK II) - PYTHAGORAS II.

^ySupported by the Romanian National Authority for Scientific Research under the contract PN 09370101.

^zPartially Supported by Ministry of Science of Montenegro, no. 05-1/3-3352.

[†]Deceased.

1 Introduction

The measurement of the charm production cross section and the derived structure function $F_2^{c\bar{c}}$ in deep-inelastic electron¹-proton scattering (DIS) at HERA allows tests of the theory of the strong interaction, quantum chromodynamics (QCD). Previous measurements [1–17] of charm production in DIS at HERA have demonstrated that charm quarks are predominantly produced by the boson gluon fusion process, which is sensitive to the gluon density in the proton. The production of charm quarks contributes up to 30% to the inclusive ep scattering cross section. The correct treatment of effects related to the charm quark contribution in perturbative QCD calculations, in particular the mass effects, is therefore important for the determination of parton distribution functions (PDFs).

At HERA several different techniques have been used to determine the charm contribution $F_2^{c\bar{c}}$ to the proton structure function F_2 . Besides the full reconstruction of a D or D^* meson [1–7, 10–12, 15, 16], the lifetime of heavy flavoured hadrons [7–9, 12, 14, 17] or the semi-leptonic decay [13] are exploited. Compared to the other methods, the measurement of D^* mesons provides a charm sample with a large signal-to-background ratio. The results presented here are based on a data sample collected by the H1 experiment, corresponding to an integrated luminosity of 348 pb^{-1} . Increased statistics, extended phase space, as well as reduced systematic uncertainties compared to the previous H1 analysis [10] make more detailed tests of pQCD predictions possible. Compared to earlier H1 analyses the phase space for the D^* meson is extended in transverse momentum from $p_T(D^*) > 1.5 \text{ GeV}$ to $p_T(D^*) > 1.25 \text{ GeV}$ and in pseudorapidity from $|\eta(D^*)| < 1.5$ to $|\eta(D^*)| < 1.8$. This extension reduces the amount of extrapolation needed for the determination of $F_2^{c\bar{c}}$.

2 QCD models and Monte Carlo simulation

The QCD models employed for data corrections and for comparison with measured cross sections are introduced in the following. Different Monte Carlo (MC) generators based on leading order (LO) QCD calculations complemented with parton showers are used to simulate detector effects in order to determine the acceptance and the efficiency for selecting DIS events with a D^* meson and to estimate the systematic uncertainties associated with the measurements. The generated events are passed through a detailed simulation of the H1 detector response based on the GEANT program [18] and through the same reconstruction and analysis algorithms as used for the data.

The MC program RAPGAP [19] is used for the generation of the direct process of boson gluon fusion to a $c\bar{c}$ pair. It uses a LO matrix element with massive charm quarks. Parton showers [20] based on the DGLAP evolution equations [21–25] model higher order QCD effects. The hadronisation of partons is performed with PYTHIA [26] which implements the Lund String Model [27, 28]. For the fragmentation of the charm quark into the D^* meson the Bowler parameterisation [29] is chosen and the longitudinal part of the fragmentation function is reweighted to the Kartvelishvili parameterisation [30]. The parameter α of the Kartvelishvili parameterisation is set to the values measured by H1 [31] which depend on the centre-of-mass energy squared \hat{s} of the hard subprocess ($\gamma g \rightarrow c\bar{c}$). The threshold between the two regions in \hat{s} is chosen such that the mean value of \hat{s} in the lower region is in agreement with the mean \hat{s} of the event sample without a jet associated with the D^* meson [31]. RAPGAP is interfaced to the HERACLES program [32] in order to simulate the radiation of a real photon from the incoming or outgoing lepton and virtual electro-weak effects. For the determination of the detector acceptance and efficiency, RAPGAP is used with the PDF set CTEQ6.6M [33] which is derived at next-to-leading order (NLO), but gives a good description of the data. Alternatively, RAPGAP is used with CTEQ6LL [34] derived at LO. The mass of the charm quark is set to $m_c = 1.5 \text{ GeV}$. The renormalisation scale μ_r and the factorisation scale μ_f are set to $\mu_r = \mu_f = \sqrt{Q^2 + 4m_c^2 + (p_T^*)^2}$, where Q^2 denotes the photon virtuality and p_T^* the transverse momentum of the charm quark in the photon-gluon centre-of-mass frame. The relevant parameter settings and their variations are summarised in Table 1.

The CASCADE [35] program is based on k_T -factorisation and the CCFM evolution equations [36–39]. In CASCADE the direct boson gluon fusion process is implemented using off-shell matrix elements convolved with a k_T -unintegrated gluon distribution of the proton. The PDF set A0 [40] is used. Time-like parton showers of the charm quark and anti-quark are implemented, but those from initial state gluons are not. The hadronisation of partons is performed in the same way as for RAPGAP. When CASCADE is used for the extrapolation to $F_2^{c\bar{c}}$, the renormalisation and factorisation scales are varied to estimate the theoretical uncertainty. For the variation of the renormalisation scale, the PDF sets A0- and A0+ are used, which were extracted with the corresponding scale variation [40]. The parameter variations used in CASCADE are also listed in Table 1.

In addition to RAPGAP and CASCADE, the data are also compared to predictions of an NLO calculation [41–46] based on collinear factorisation and the DGLAP evolution equations. This calculation assumes three active flavours (u, d, s) in the proton (fixed-flavour-number scheme: FFNS) and massive charm quarks are produced dynamically via

¹In this paper “electron” is used to denote both electron and positron.

Table 1 Parameters used in the MC simulations. The central choice of the renormalisation (factorisation) scale is denoted by $\mu_{r,0}$ ($\mu_{f,0}$). The invariant mass squared and the transverse momentum squared of the $c\bar{c}$ pair are denoted by \hat{s} and Q_T^2 , respectively, m_c is the charm quark mass and p_T^* and p_T are the transverse momentum of the charm quark in the photon-gluon centre-of-mass frame and in the electron-proton centre-of-mass frame, respectively. α is the fragmentation parameter in the Kartvelishvili parameterisation. Two values of α in two regions of \hat{s} with the boundary $\hat{s}_{\text{threshold}}$ are used [31]. For CASCADE different PDF sets are available which were determined for a variation of the renormalisation scale by a factor of 1/2 or 2. These are used consistently for the μ_r variation here

Parameter name	Central value	Variation
RAPGAP		
Charm mass	$m_c = 1.5 \text{ GeV}$	
Renormalisation scale	$\mu_r = \sqrt{Q^2 + 4m_c^2 + (p_T^*)^2}$	
Factorisation scale	$\mu_f = \sqrt{Q^2 + 4m_c^2 + (p_T^*)^2}$	
Fragmentation	$\alpha = 10.3$ for $\hat{s} < \hat{s}_{\text{threshold}}$ $\alpha = 4.4$ for $\hat{s} > \hat{s}_{\text{threshold}}$ $\hat{s}_{\text{threshold}} = 70 \text{ GeV}^2$	$8.7 < \alpha < 12.2$ $3.9 < \alpha < 5.0$ $50 < \hat{s}_{\text{threshold}} < 90 \text{ GeV}^2$
PDF	CTEQ6.6M	CTEQ6LL
CASCADE		
Charm mass	$m_c = 1.5 \text{ GeV}$	
Renormalisation scale	$\mu_{r,0} = \sqrt{Q^2 + 4m_c^2 + p_T^2}$	$1/2 < \mu_r/\mu_{r,0} < 2$
Factorisation scale	$\mu_{f,0} = \sqrt{\hat{s} + Q_T^2}$	$1/2 < \mu_f/\mu_{f,0} < 2$
Fragmentation	$\alpha = 8.4$ for $\hat{s} < \hat{s}_{\text{threshold}}$ $\alpha = 4.5$ for $\hat{s} > \hat{s}_{\text{threshold}}$ $\hat{s}_{\text{threshold}} = 70 \text{ GeV}^2$	$7.3 < \alpha < 9.7$ $3.9 < \alpha < 5.1$ $50 < \hat{s}_{\text{threshold}} < 90 \text{ GeV}^2$
PDF	A0	μ_r variation: A0-, A0+

Table 2 Parameter variations used for the uncertainty estimation of the NLO calculations. The central choice of the renormalisation (factorisation) scale is denoted by $\mu_{r,0}$ ($\mu_{f,0}$). m_c is the charm quark mass and α is the fragmentation parameter in the Kartvelishvili parameterisation. In the two regions of \hat{s} , separated by the boundary $\hat{s}_{\text{threshold}}$, different values of α are used [31]

Parameter name	Central value	Variation
HVQDIS		
Charm mass	$m_c = 1.5 \text{ GeV}$	$1.3 < m_c < 1.7 \text{ GeV}$
Renormalisation scale	$\mu_{r,0} = \sqrt{Q^2 + 4m_c^2}$	$1/2 < \mu_r/\mu_{r,0} < 2$
Factorisation scale	$\mu_{f,0} = \sqrt{Q^2 + 4m_c^2}$	$1/2 < \mu_f/\mu_{f,0} < 2$
Fragmentation	$\alpha = 6.1$ for $\hat{s} < \hat{s}_{\text{threshold}}$ $\alpha = 3.3$ for $\hat{s} > \hat{s}_{\text{threshold}}$ $\hat{s}_{\text{threshold}} = 70 \text{ GeV}^2$	$5.3 < \alpha < 7.0$ $2.9 < \alpha < 3.7$ $50 < \hat{s}_{\text{threshold}} < 90 \text{ GeV}^2$
PDF	CT10f3	MSTW2008f3
Fragmentation fraction	$f(c \rightarrow D^*) = 23.8 \pm 0.8\%$ [49]	
ZM-VFNS		
Charm mass	$m_c = 1.5 \text{ GeV}$	
Renormalisation scale	$\mu_{r,0} = \sqrt{(Q^2 + (p_T^*)^2)/2}$	$1/2 < \mu_r/\mu_{r,0} < 2$
Factorisation scale	$\mu_{f,0} = \sqrt{(Q^2 + (p_T^*)^2)/2}$	$1/2 < \mu_f/\mu_{f,0} < 2$
Fragmentation	KKKS08 [53]	
PDF	CTEQ6.6M	

boson gluon fusion. The predictions are calculated using the program HVQDIS [45, 46]. Corresponding fixed-flavour NLO parton density functions of the proton, CT10f3 [47] (with the strong coupling set to $\alpha_S(M_Z) = 0.106$) and the NLO variant of MSTW2008f3 [48], are used. Charm quarks are fragmented in the γp centre-of-mass frame into D^* mesons using the Kartvelishvili [30] parameterisation for the fragmentation function with the value of the para-

meter α as measured by H1 [31]. The renormalisation and factorisation scales are set to $\mu_r = \mu_f = \sqrt{Q^2 + 4m_c^2}$. The value used for the charm mass is 1.5 GeV. To obtain the theoretical systematic uncertainty for the extrapolation to $F_2^{c\bar{c}}$ the parameters are varied according to Table 2. Each of the variations is performed independently. The resulting uncertainties are added in quadrature to obtain a conservative estimate of the total theoretical uncertainty.

The results are also compared with a NLO calculation [50–52] based on the zero-mass variable-flavour-number scheme (ZM-VFNS), where the charm quark is considered as a massless constituent of the proton. This calculation is only valid for a sufficiently large transverse momentum of the D^* meson $p_T^*(D^*)$ in the γp centre-of-mass frame. For the comparison to this prediction the analysis is therefore restricted to $p_T^*(D^*) > 2$ GeV. The ZM-VFNS uses the fragmentation function determined in [53]. The scales are chosen to be $\mu_r = \mu_f = \sqrt{(Q^2 + (p_T^*)^2)/2}$.

3 H1 detector

A detailed description of the H1 detector can be found elsewhere [54–56]. Only the components essential to the present analysis are described here. The origin of the H1 coordinate system is the nominal ep interaction point. The direction of the proton beam defines the positive z -axis (forward direction). Transverse momenta are measured in the x – y plane. Polar (θ) and azimuthal (ϕ) angles are measured with respect to this reference system. The pseudo-rapidity is defined as $\eta = -\ln \tan(\theta/2)$.

Charged particles are measured within the central tracking detector (CTD) in the pseudo-rapidity range $-1.85 < \eta < 1.85$. The CTD consists of two large cylindrical jet chambers (CJCs), surrounding the silicon vertex detector CST [57, 58]. The CJCs are separated by a drift chamber which improves the z coordinate reconstruction. A multi-wire proportional chamber [59], which is mainly used in the trigger, is situated inside the inner CJC. These detectors are arranged concentrically around the interaction region in a magnetic field of 1.16 T. The trajectories of charged particles are measured with a transverse momentum resolution of $\sigma(p_T)/p_T \approx 0.5\% p_T/\text{GeV} \oplus 1.5\%$ [60]. The interaction vertex is reconstructed from CTD tracks. The CTD also provides triggering information based on track segments measured in the CJCs [61–63] and a measurement of the specific ionisation energy loss dE/dx of charged particles. The forward tracking detector measures tracks of charged particles at smaller polar angle ($1.5 < \eta < 2.8$) than the central tracker.

Charged and neutral particles are measured in the liquid argon (LAr) calorimeter, which surrounds the tracking chambers and covers the range $-1.5 < \eta < 3.4$ with full azimuthal acceptance. Electromagnetic shower energies are measured with a precision of $\sigma(E)/E = 12\%/\sqrt{E/\text{GeV}} \oplus 1\%$ and hadronic energies with $\sigma(E)/E = 50\%/\sqrt{E/\text{GeV}} \oplus 2\%$, as determined in test beam measurements [64, 65]. A lead-scintillating fibre calorimeter (SpaCal) [56] covering the backward region $-4.0 < \eta < -1.4$ completes the measurement of charged and neutral particles. In this analysis the SpaCal is used in particular for the identification and

reconstruction of the scattered electron. For electrons a relative energy resolution of $\sigma(E)/E = 7\%/\sqrt{E/\text{GeV}} \oplus 1\%$ is achieved, as determined in test beam measurements [66]. The SpaCal provides energy and time-of-flight information used for triggering purposes. A Backward Proportional Chamber (BPC) in front of the SpaCal is used to improve the angular measurement of the scattered electron.

The hadronic final state is reconstructed using an energy flow algorithm which combines charged particles measured in the CTD and the forward tracking detector with information from the SpaCal and LAr calorimeters [67, 68].

The luminosity determination is based on the measurement of the Bethe-Heitler process ($ep \rightarrow ep\gamma$) where the photon is detected in a calorimeter located at $z = -103$ m downstream of the interaction region in the electron beam direction.

4 Event selection and signal extraction

The data sample corresponds to an integrated luminosity $\mathcal{L} = 348 \text{ pb}^{-1}$ and was recorded with the H1 detector in e^+p (185 pb^{-1}) and e^-p interactions (163 pb^{-1}) in the years 2004 to 2007. During this period electrons at an energy of 27.6 GeV were collided with protons at 920 GeV. The events were triggered by a local energy deposit in the SpaCal in coincidence with at least one track in the CTD, with an overall trigger efficiency of 98%.

DIS events are selected by requiring a high energy electromagnetic cluster in the SpaCal which is consistent with resulting from the scattered electron. The event kinematics including the photon virtuality Q^2 , the Bjorken scaling variable x and the inelasticity variable y are reconstructed with the $e\Sigma$ method [69], which uses information from the scattered electron and the hadronic final state and provides good resolution in the covered y range. The kinematic region for the photon virtuality is restricted to $5 < Q^2 < 100 \text{ GeV}^2$ corresponding to the geometric acceptance of the SpaCal. In order to ensure a high trigger efficiency, the energy of the electron candidate is required to fulfil $E'_e > 10 \text{ GeV}$. The inelasticity is restricted to the range $0.02 < y < 0.7$.

Charm production is identified by the reconstruction of D^* mesons using the decay channel $D^{*\pm} \rightarrow D^0\pi_s^\pm \rightarrow K^\mp\pi^\pm\pi_s^\pm$ which has a branching fraction $\mathcal{BR} = 2.63 \pm 0.04\%$ [70]. The tracks of the decay particles are reconstructed in the CTD. The invariant mass of the $K^\mp\pi^\pm$ system is required to be consistent with the D^0 mass [70] within $\pm 80 \text{ MeV}$. A loose particle identification criterion is applied to the kaon candidates using the measurement of the specific energy loss, dE/dx , in the CTD. This improves the signal-to-background ratio, especially at low transverse momenta of the D^* meson. The kinematic range of the measurement is summarised in Table 3. Details of the selection are described in [71].

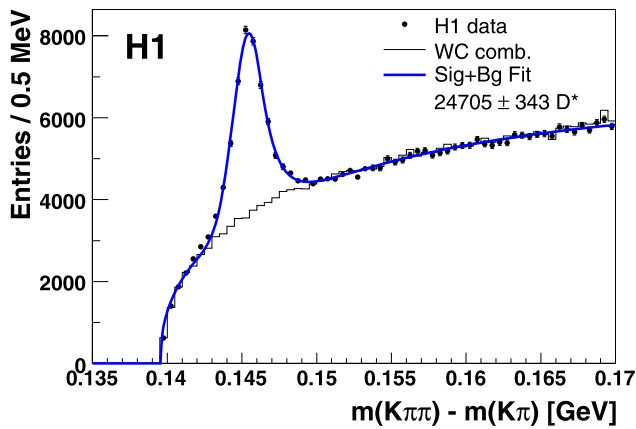


Fig. 1 Distribution of the mass difference $\Delta m = m(K^\pm\pi^\pm\pi_s^\pm) - m(K^\mp\pi^\pm)$ for D^* candidates in the kinematic range of $5 < Q^2 < 100 \text{ GeV}^2$, $0.02 < y < 0.7$, $|\eta(D^*)| < 1.8$ and $p_T(D^*) > 1.25 \text{ GeV}$. The histogram shows the wrong charge combinations, $K^\pm\pi^\pm\pi_s^\mp$. The solid line represents the result of the fit described in the text

$D^{*\pm}$ candidates are selected using the mass difference method [72]. The distribution of the mass difference $\Delta m = m(K^\mp\pi^\pm\pi_s^\pm) - m(K^\mp\pi^\pm)$ is shown in Fig. 1. A clear signal peak around the nominal mass difference of 145.4 MeV [70] is observed.

The wrong charge combinations, defined as $K^\pm\pi^\pm\pi_s^\mp$ with $K^\pm\pi^\pm$ pairs in the accepted D^0 mass range, are used to constrain the shape of the combinatorial background in the signal region. The number of D^* mesons is determined in each analysis bin by a simultaneous fit to the right and the wrong charge Δm distribution. As the signal has a tail towards larger Δm values, the asymmetric Crystal Ball function [73] is used for the signal description. The shape of the background is parameterised with the Granet function [74]. An unbinned extended log likelihood fit [75] is performed using the RooFit framework [76].

The fit to the complete data set yields 24705 ± 343 D^* mesons. This represents an increase in statistics of an order of magnitude compared to the previous analysis [10]. For each analysis bin the fit to the Δm spectrum uses the two parameters describing the signal asymmetry obtained from the fit to the complete data set. The width of the peak varies in dependence of the D^* kinematics and is therefore treated as a free parameter of the fit.

5 Cross section determination and systematic errors

The following formula is used to calculate the inclusive D^* meson production cross section at the Born level in the visible kinematic range defined in Table 3:

$$\sigma_{\text{vis}}(ep \rightarrow eD^{*\pm}X) = \frac{N(D^{*\pm}) \cdot (1 - r)}{\mathcal{L} \cdot \mathcal{BR}(D^* \rightarrow K\pi\pi_s) \cdot (1 + \delta_{\text{rad}})} \quad (1)$$

Table 3 Definition of the kinematic range of the present measurement

Photon virtuality Q^2	$5 < Q^2 < 100 \text{ GeV}^2$
Inelasticity y	$0.02 < y < 0.7$
Pseudo-rapidity of $D^{*\pm}$	$-1.8 < \eta(D^*) < 1.8$
Transverse momentum of $D^{*\pm}$	$p_T(D^*) > 1.25 \text{ GeV}$

Table 4 Summary of all sources of systematic uncertainties and their effect on the D^* production cross section with the breakdown into bin-to-bin uncorrelated and bin-to-bin correlated sources

Uncorrelated uncertainties	
Signal extraction	2%
Radiative correction	2%
Trigger efficiency	1%
D^0 meson mass cut	1.5%
Reflections	1.0%
Photoproduction background	< 0.2%
dE/dx cut	2%
Correlated uncertainties	
Track efficiency	4.1%
Luminosity	3.2%
Branching ratio	1.5%
Model	2.1%
PDF	1%
Fragmentation	2.6%
Electron energy scale	1.3%
Electron angle θ	1.3%
Hadronic energy scale	0.3%
Total systematic uncertainty	7.6%

Here $N(D^{*\pm})$ is the number of D^* mesons obtained using an unfolding procedure defined below, r is the contribution from reflections from other decay modes of the D^0 meson, \mathcal{L} is the integrated luminosity, \mathcal{BR} is the branching ratio and δ_{rad} denotes the QED radiative corrections. For the differential measurements the cross section is also divided by the bin width. No bin centre correction is applied.

To obtain $N(D^*)$ in each measurement bin, the data are corrected for detector effects including the trigger efficiency by means of regularised matrix unfolding [77–80]. The response matrix \mathbf{A} which reflects the acceptance and the resolution of the H1 detector relates the distributions \vec{y}_{rec} of reconstructed variables to distributions \vec{x}_{true} of variables at the generator level, $\mathbf{A}\vec{x}_{\text{true}} = \vec{y}_{\text{rec}}$. Each matrix element A_{ij} is the probability for an event originating from bin j of \vec{x}_{true} to be measured in bin i of \vec{y}_{rec} . The response matrix is determined from simulation and has twice as many bins at the reconstruction level as at the generator level in order to provide detailed information on the probability distribution and to improve thereby the accuracy of the unfolding procedure. The procedure reduces statistical correlations between

Table 5 Differential D^* cross section as a function of Q^2 , y and x in the kinematic range of $5 < Q^2 < 100 \text{ GeV}^2$, $0.02 < y < 0.7$, $|\eta(D^*)| < 1.8$ and $p_T(D^*) > 1.25 \text{ GeV}$. The first quoted uncertainty is statistical and the second is systematic

Q^2 range [GeV ²]		$d\sigma/dQ^2$ [nb/GeV ²]			$d\sigma/dQ^2$ [nb/GeV ²] for $p_T^*(D^*) > 2.0 \text{ GeV}$		
5.0	6.0	0.782	± 0.048	$\pm_{0.057}^{0.058}$	0.317	± 0.023	$\pm_{0.022}^{0.023}$
6.0	8.0	0.538	± 0.022	$\pm_{0.039}^{0.039}$	0.237	± 0.012	$\pm_{0.018}^{0.018}$
8.0	10.0	0.384	± 0.018	$\pm_{0.028}^{0.028}$	0.1568	± 0.0094	$\pm_{0.0110}^{0.0115}$
10.0	13.0	0.249	± 0.011	$\pm_{0.018}^{0.018}$	0.1156	± 0.0063	$\pm_{0.0084}^{0.0085}$
13.0	19.0	0.1549	± 0.0057	$\pm_{0.0110}^{0.0109}$	0.0695	± 0.0031	$\pm_{0.0050}^{0.0051}$
19.0	27.5	0.0874	± 0.0038	$\pm_{0.0062}^{0.0062}$	0.0350	± 0.0019	$\pm_{0.0025}^{0.0025}$
27.5	40.0	0.0463	± 0.0022	$\pm_{0.0032}^{0.0032}$	0.0206	± 0.0011	$\pm_{0.0015}^{0.0015}$
40.0	60.0	0.0188	± 0.0013	$\pm_{0.0014}^{0.0014}$	0.00856	± 0.00067	$\pm_{0.00059}^{0.00059}$
60.0	100.0	0.00824	± 0.00057	$\pm_{0.00057}^{0.00058}$	0.00478	± 0.00037	$\pm_{0.00034}^{0.00034}$

y range		$d\sigma/dy$ [nb]			$d\sigma/dy$ [nb] for $p_T^*(D^*) > 2.0 \text{ GeV}$		
0.02	0.05	21.67	± 1.04	$\pm_{2.83}^{2.53}$	4.75	± 0.40	$\pm_{0.65}^{0.81}$
0.05	0.09	20.97	± 0.94	$\pm_{1.79}^{1.51}$	7.14	± 0.41	$\pm_{0.71}^{0.68}$
0.09	0.13	20.05	± 0.97	$\pm_{1.58}^{1.48}$	7.61	± 0.46	$\pm_{0.65}^{0.68}$
0.13	0.18	14.63	± 0.80	$\pm_{1.03}^{1.04}$	6.79	± 0.50	$\pm_{0.52}^{0.52}$
0.18	0.26	12.61	± 0.54	$\pm_{0.90}^{0.91}$	5.01	± 0.25	$\pm_{0.38}^{0.39}$
0.26	0.36	8.39	± 0.43	$\pm_{0.63}^{0.72}$	4.25	± 0.20	$\pm_{0.32}^{0.32}$
0.36	0.50	5.87	± 0.31	$\pm_{0.47}^{0.63}$	2.96	± 0.17	$\pm_{0.24}^{0.25}$
0.50	0.70	3.00	± 0.27	$\pm_{0.30}^{0.32}$	1.83	± 0.16	$\pm_{0.18}^{0.19}$

x range		$d\sigma/dx$ [nb]			$d\sigma/dx$ [nb] for $p_T^*(D^*) > 2.0 \text{ GeV}$		
0.00007	0.00020	4990	± 300	\pm_{390}^{440}	2970	± 180	\pm_{210}^{230}
0.00020	0.00035	6020	± 280	\pm_{440}^{460}	3060	± 160	\pm_{210}^{220}
0.00035	0.00060	4180	± 170	\pm_{310}^{320}	1994	± 93	\pm_{141}^{143}
0.00060	0.00100	2631	± 109	\pm_{188}^{190}	1172	± 57	\pm_{86}^{87}
0.00100	0.00170	1540	± 61	\pm_{108}^{107}	586	± 31	\pm_{42}^{42}
0.00170	0.00330	579	± 24	\pm_{45}^{44}	235	± 12	\pm_{22}^{22}
0.00330	0.05000	13.24	± 0.61	$\pm_{1.33}^{1.17}$	4.20	± 0.24	$\pm_{0.45}^{0.45}$

neighbouring bins and the influence of model assumptions in the cross section determination. Additional bins outside of the kinematic range of this measurement are used to provide constraints on the migrations into the measured phase space.

The measured D^* cross section includes decays from B hadrons to D^* mesons which are expected to contribute to less than 2%. For the determination of $F_2^{c\bar{c}}$ the beauty contribution as calculated with HVQDIS is subtracted.

For the present analysis the systematic error dominates over the statistical uncertainty for almost the whole phase space. The measurement is statistically limited only for large

transverse momenta or large photon virtualities. The systematic uncertainties are determined in each bin separately and are summarised in Table 4 for the total cross section. They are divided into uncertainties which are bin-to-bin uncorrelated and uncertainties which are correlated between the bins. The uncertainties in the following are given in percent of the cross section values.

The following sources for bin-to-bin uncorrelated systematic errors are considered:

Signal extraction: Using different parameterisations for the signal and background shapes [71] the systematic uncertainty on the signal extraction is estimated to be 2%.

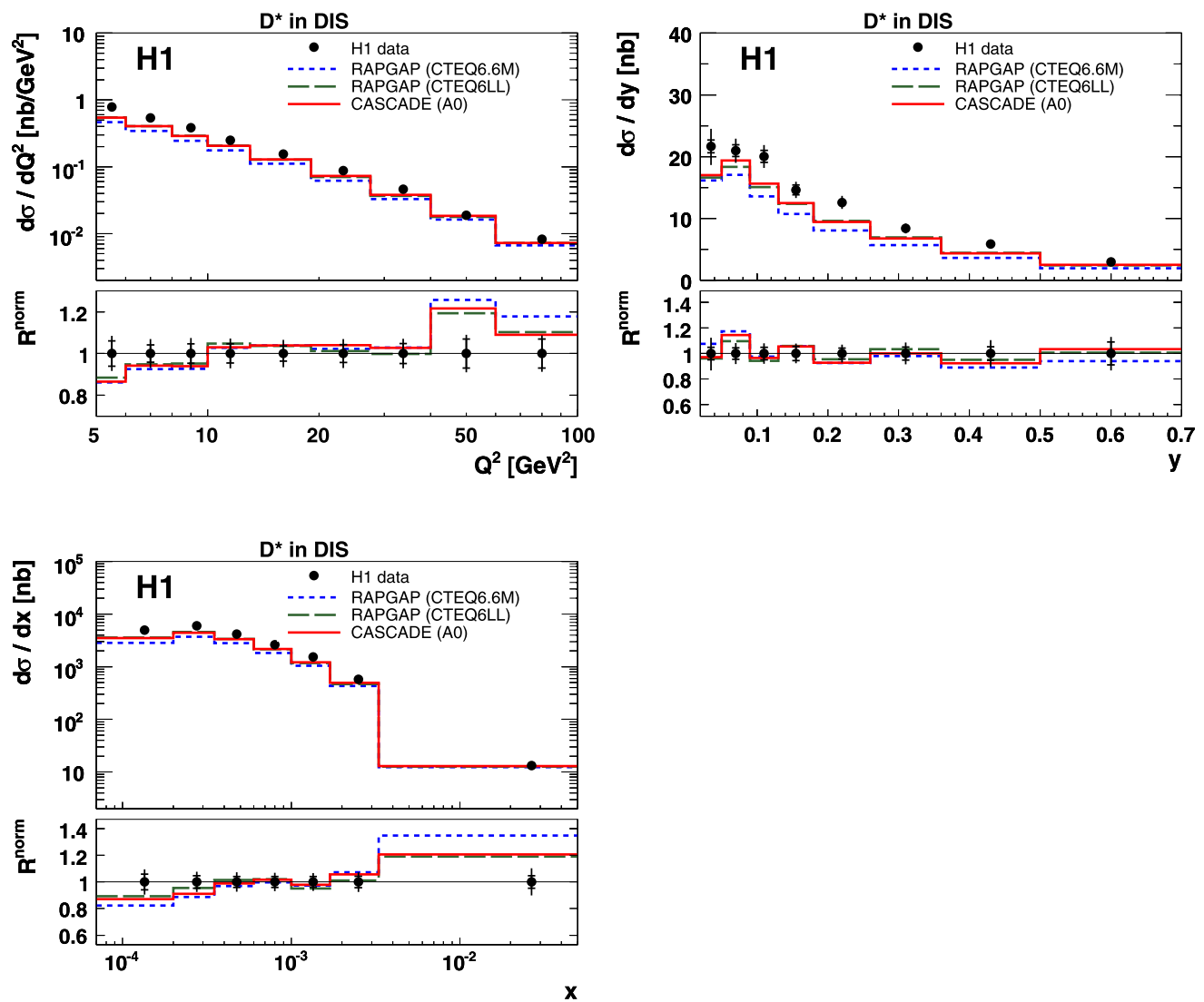


Fig. 2 Differential D^* cross section as a function of the photon virtuality Q^2 , the inelasticity y and Bjorken x . The measurements correspond to the kinematic range of $5 < Q^2 < 100 \text{ GeV}^2$, $0.02 < y < 0.7$, $|\eta(D^*)| < 1.8$ and $p_T(D^*) > 1.25 \text{ GeV}$. The data are shown as *points*, the *inner error bars* show the statistical error, the *outer error bars* represent the statistical and systematic errors added in quadrature. The

data are compared to predictions by the MC program RAPGAP with two different proton parton densities and by the MC program CASCADE. In the *lower part* of the *figures* the normalised ratio R^{norm} of theory to data (3) is shown, which has reduced normalisation uncertainties

Radiative corrections: For the correction of the measured cross section to the Born level, the HERACLES interface to RAPGAP is used. The corrections are of the order of 2.5%. An uncertainty of 2% is assigned [17].

Trigger efficiency: The efficiency of the trigger conditions requiring an energy deposition in the SpaCal and a central track is at least 95%. The combined uncertainty is estimated to be 1%.

D^0 mass cut: The invariant mass resolution of the data is not fully reproduced by the MC simulation, leading to different efficiencies of the D^0 mass cut. The difference is evaluated by comparing the width of the D^0 signal in data

and MC and extrapolating to the region outside of the mass cut assuming a Gaussian distribution [71]. The dependence on the D^* kinematics is studied, and the maximum difference of 1.5% is assigned as uncertainty.

Reflections: The amount of reflections r from decay modes of the D^0 meson other than $D^0 \rightarrow K^\mp \pi^\pm$ is determined using a RAPGAP MC sample of inclusive charm events and is found to amount to 3.8%. The dependence of r on kinematic quantities is studied in the simulation and found to be constant within 1%, a value which is used as the systematic uncertainty.

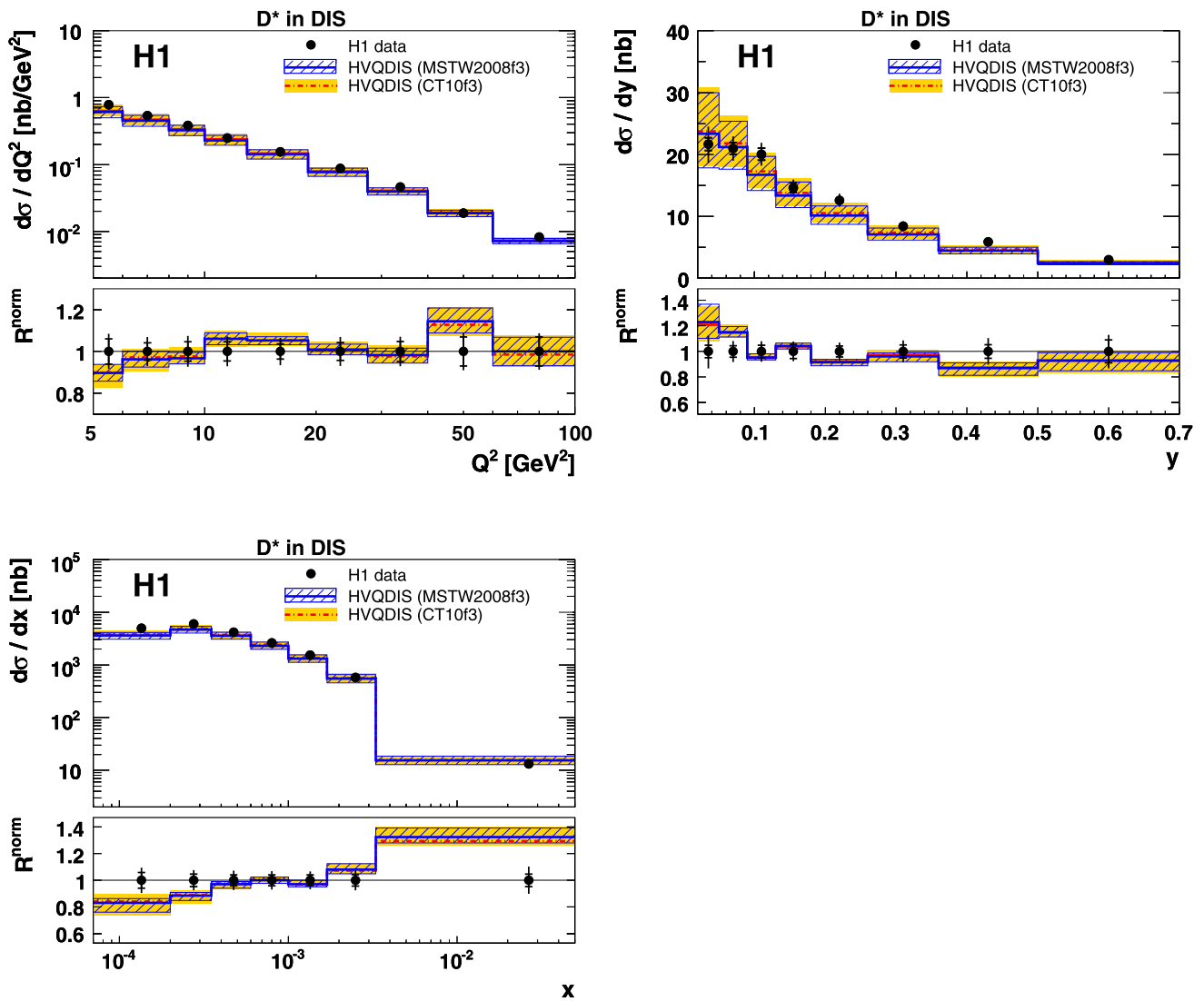


Fig. 3 Differential D^* cross section as a function of the photon virtuality Q^2 , the inelasticity y and Bjorken x . The measurements correspond to the kinematic range of $5 < Q^2 < 100 \text{ GeV}^2$, $0.02 < y < 0.7$, $|\eta(D^*)| < 1.8$ and $p_T(D^*) > 1.25 \text{ GeV}$. The data are shown as *points*, the *inner error bars* show the statistical error, the *outer error bars* represent the statistical and systematic errors added in quadrature. The

data are compared to predictions by the next-to-leading order calculation HVQDIS with two different proton parton densities. The *bands* indicate the theoretical uncertainties (Table 2). In the *lower part of the figures* the normalised ratio R^{norm} of theory to data (3) is shown, which has reduced normalisation uncertainties

Photoproduction background: The photoproduction background is estimated using a PYTHIA photoproduction MC sample to be less than 0.2%, which is used as systematic uncertainty.

dE/dx cut: The loss of D^* signal events due to the dE/dx requirement on the kaon track amounts to 3.4% in data. The dE/dx cut is not applied in the simulation, but corrected for in the data by a global factor. The dependence of the cut efficiency on kinematic variables is studied and found to be within 2%, which is used as systematic uncertainty.

Where appropriate, the effect of the bin-to-bin correlated systematic uncertainties is evaluated by changing the response matrix and repeating the unfolding procedure. The following correlated error sources are considered:

Track finding efficiency: The systematic error on the track efficiency of 4.1% per D^* meson is the dominant error of this measurement. It arises from two contributions: (i) The comparison of the track finding efficiency in data and simulation leads to an error of 2% for the slow pion track and 1% for the tracks of the D^0 daughter particles and is assumed to be correlated between the decay particles; (ii) the efficiency with which a track can be fitted to the event ver-

Table 6 Differential D^* cross section as a function of $p_T(D^*)$, $\eta(D^*)$, $p_T^*(D^*)$ and $z(D^*)$ in the kinematic range of $5 < Q^2 < 100 \text{ GeV}^2$, $0.02 < y < 0.7$, $|\eta(D^*)| < 1.8$, $p_T(D^*) > 1.25 \text{ GeV}$. The first quoted uncertainty is statistical and the second is systematic

p_T range [GeV]		$d\sigma/dp_T$ [nb/GeV]			$d\sigma/dp_T$ [nb/GeV] for $p_T^*(D^*) > 2.0 \text{ GeV}$		
1.25	1.60	2.55	± 0.21	$\pm_{0.18}^{0.18}$	0.334	± 0.042	$\pm_{0.035}^{0.035}$
1.60	1.88	2.88	± 0.19	$\pm_{0.20}^{0.20}$	0.436	± 0.055	$\pm_{0.042}^{0.041}$
1.88	2.28	2.68	± 0.11	$\pm_{0.19}^{0.19}$	0.853	± 0.057	$\pm_{0.062}^{0.061}$
2.28	2.68	2.147	± 0.086	$\pm_{0.149}^{0.149}$	0.935	± 0.057	$\pm_{0.086}^{0.086}$
2.68	3.08	1.538	± 0.058	$\pm_{0.107}^{0.107}$	0.744	± 0.047	$\pm_{0.065}^{0.065}$
3.08	3.50	1.362	± 0.047	$\pm_{0.094}^{0.094}$	0.806	± 0.042	$\pm_{0.061}^{0.061}$
3.50	4.00	0.924	± 0.032	$\pm_{0.064}^{0.064}$	0.620	± 0.033	$\pm_{0.046}^{0.046}$
4.00	4.75	0.630	± 0.020	$\pm_{0.043}^{0.043}$	0.443	± 0.022	$\pm_{0.031}^{0.031}$
4.75	6.00	0.2987	± 0.0098	$\pm_{0.0208}^{0.0209}$	0.239	± 0.012	$\pm_{0.016}^{0.016}$
6.00	8.00	0.0883	± 0.0039	$\pm_{0.0067}^{0.0070}$	0.0769	± 0.0042	$\pm_{0.0054}^{0.0056}$
8.00	11.00	0.0217	± 0.0015	$\pm_{0.0016}^{0.0016}$	0.0210	± 0.0016	$\pm_{0.0014}^{0.0015}$
11.00	20.00	0.00183	± 0.00034	$\pm_{0.00022}^{0.00023}$	0.00188	± 0.00032	$\pm_{0.00013}^{0.00015}$

η range		$d\sigma/d\eta$ [nb]			$d\sigma/d\eta$ [nb] for $p_T^*(D^*) > 2.0 \text{ GeV}$		
-1.80	-1.56	1.19	± 0.14	$\pm_{0.09}^{0.09}$	0.460	± 0.078	$\pm_{0.047}^{0.061}$
-1.56	-1.32	1.362	± 0.097	$\pm_{0.102}^{0.101}$	0.500	± 0.051	$\pm_{0.042}^{0.050}$
-1.32	-1.08	1.418	± 0.071	$\pm_{0.100}^{0.102}$	0.592	± 0.037	$\pm_{0.043}^{0.068}$
-1.08	-0.84	1.635	± 0.071	$\pm_{0.116}^{0.118}$	0.672	± 0.036	$\pm_{0.047}^{0.062}$
-0.84	-0.60	1.629	± 0.069	$\pm_{0.115}^{0.115}$	0.728	± 0.038	$\pm_{0.053}^{0.056}$
-0.60	-0.36	1.829	± 0.073	$\pm_{0.130}^{0.130}$	0.814	± 0.041	$\pm_{0.058}^{0.083}$
-0.36	-0.12	1.731	± 0.071	$\pm_{0.121}^{0.123}$	0.836	± 0.042	$\pm_{0.064}^{0.077}$
-0.12	0.12	1.878	± 0.081	$\pm_{0.131}^{0.131}$	0.894	± 0.048	$\pm_{0.067}^{0.070}$
0.12	0.36	1.763	± 0.078	$\pm_{0.123}^{0.123}$	0.824	± 0.044	$\pm_{0.060}^{0.065}$
0.36	0.60	1.927	± 0.090	$\pm_{0.136}^{0.136}$	0.947	± 0.048	$\pm_{0.068}^{0.074}$
0.60	0.84	1.880	± 0.095	$\pm_{0.133}^{0.134}$	0.931	± 0.050	$\pm_{0.066}^{0.075}$
0.84	1.08	2.025	± 0.097	$\pm_{0.142}^{0.144}$	0.939	± 0.049	$\pm_{0.065}^{0.067}$
1.08	1.32	2.19	± 0.12	$\pm_{0.16}^{0.16}$	0.856	± 0.056	$\pm_{0.059}^{0.062}$
1.32	1.56	1.97	± 0.17	$\pm_{0.14}^{0.14}$	0.764	± 0.077	$\pm_{0.055}^{0.055}$
1.56	1.80	1.93	± 0.24	$\pm_{0.14}^{0.14}$	0.876	± 0.107	$\pm_{0.069}^{0.075}$

p_T^* range [GeV]		$d\sigma/dp_T^*$ [nb/GeV]		
0.300	0.700	1.26	± 0.16	$\pm_{0.18}^{0.18}$
0.700	1.125	1.83	± 0.14	$\pm_{0.21}^{0.21}$
1.125	1.500	2.22	± 0.15	$\pm_{0.19}^{0.18}$
1.500	1.880	2.39	± 0.14	$\pm_{0.17}^{0.17}$
1.880	2.280	2.02	± 0.11	$\pm_{0.14}^{0.14}$
2.280	2.680	1.417	± 0.086	$\pm_{0.099}^{0.099}$
2.680	3.080	1.055	± 0.063	$\pm_{0.074}^{0.074}$
3.080	3.500	0.711	± 0.045	$\pm_{0.050}^{0.051}$
3.500	4.250	0.453	± 0.022	$\pm_{0.033}^{0.033}$
4.250	6.000	0.2028	± 0.0080	$\pm_{0.0162}^{0.0173}$
6.000	11.000	0.0287	± 0.0017	$\pm_{0.0022}^{0.0023}$
11.000	20.000	0.00278	± 0.00062	$\pm_{0.00028}^{0.00030}$

Table 6 (Continued)

z range		dσ/dz [nb]			dσ/dz [nb] for p _T [*] (D [*]) > 2.0 GeV		
0.000	0.100	5.12	±0.59	± ^{0.45} _{0.40}	1.72	±0.26	± ^{0.59} _{0.60}
0.100	0.200	9.42	±0.59	± ^{0.86} _{0.80}	4.52	±0.29	± ^{0.41} _{0.40}
0.200	0.325	10.36	±0.48	± ^{0.86} _{0.78}	5.44	±0.24	± ^{0.40} _{0.40}
0.325	0.450	9.66	±0.41	± ^{0.77} _{0.72}	4.91	±0.21	± ^{0.48} _{0.47}
0.450	0.575	9.30	±0.36	± ^{0.68} _{0.71}	3.71	±0.16	± ^{0.42} _{0.42}
0.575	0.800	4.97	±0.16	± ^{0.46} _{0.61}	1.156	±0.066	± ^{0.167} _{0.163}
0.800	1.000	1.086	±0.082	± ^{0.305} _{0.266}	0.347	±0.038	± ^{0.077} _{0.080}

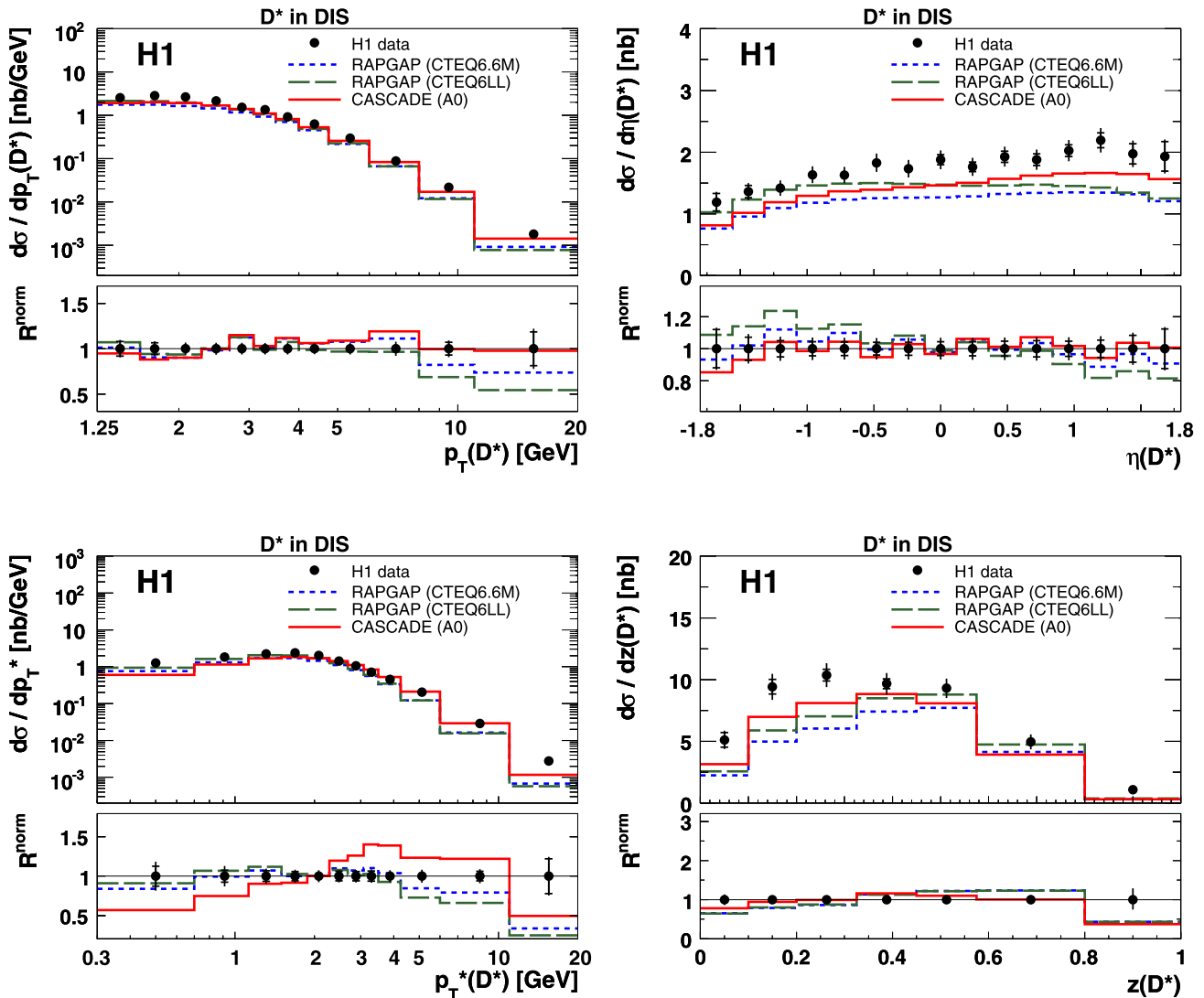


Fig. 4 Differential D^* cross section as a function of the transverse momentum $p_T(D^*)$ and pseudo-rapidity $\eta(D^*)$ in the laboratory frame, the transverse momentum $p_T^*(D^*)$ in the $\gamma\gamma$ centre-of-mass frame and the D^* inelasticity $z(D^*)$. The measurements correspond to the kinematic range of $5 < Q^2 < 100 \text{ GeV}^2$, $0.02 < y < 0.7$ and $|\eta(D^*)| < 1.8$ and $p_T(D^*) > 1.25 \text{ GeV}$. The data are shown as points, the inner error

bars show the statistical error, the outer error bars represent the statistical and systematic errors added in quadrature. The data are compared to predictions by the MC program RAPGAP with two different proton parton densities and by the MC program CASCADE. In the lower part of the figures the normalised ratio R^{norm} of theory to data (3) is shown, which has reduced normalisation uncertainties

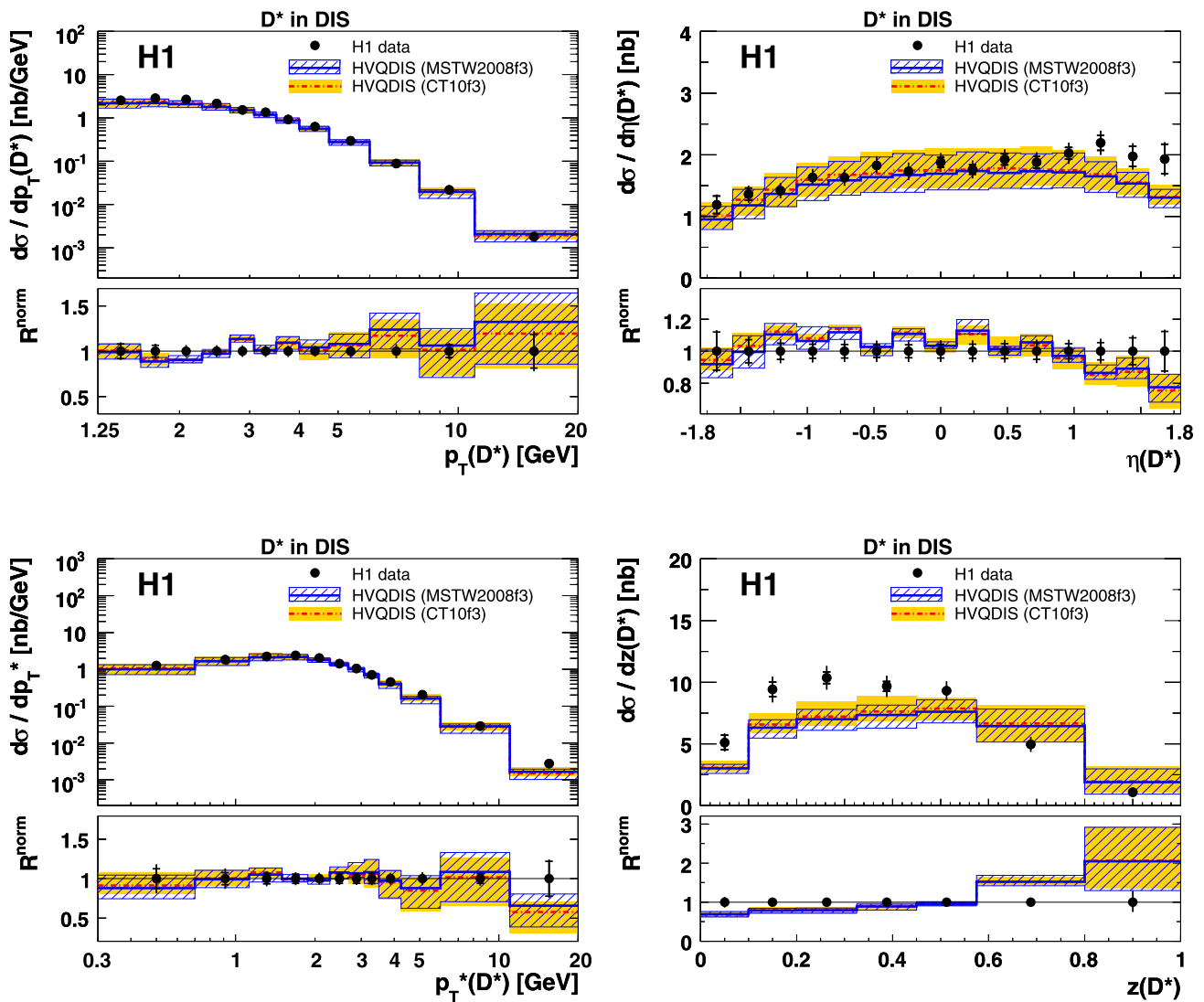


Fig. 5 Differential D^* cross section as a function of the transverse momentum $p_T(D^*)$ and pseudo-rapidity $\eta(D^*)$ in the laboratory frame, the transverse momentum $p_T^*(D^*)$ in the γp centre-of-mass frame and the D^* inelasticity $z(D^*)$. The measurements correspond to the kinematic range of $5 < Q^2 < 100 \text{ GeV}^2$, $0.02 < y < 0.7$ and $|\eta(D^*)| < 1.8$ and $p_T(D^*) > 1.25 \text{ GeV}$. The data are shown as *points*, the *inner error bars* show the statistical error, the *outer error bars*

represent the statistical and systematic errors added in quadrature. The data are compared to predictions by the next-to-leading order calculation HVQDIS with two different proton parton densities. The *bands* indicate the theoretical uncertainties (Table 2). In the *lower part* of the *figures* the normalised ratio R^{norm} of theory to data (3) is shown, which has reduced normalisation uncertainties

tex leads to a systematic error of 1% per D^* meson. The uncertainty on the track finding efficiency is considered to be half correlated between the bins of the measurement.

Luminosity: The systematic error on the luminosity measurement is estimated to be 3.2%.

Branching ratio: The uncertainty on the branching ratio of the D^* meson is 1.5% [70].

Model: The parton shower model uncertainty is on average 2%, estimated by taking the difference in cross section obtained using RAPGAP or CASCADE for the data correction.

PDF: Using different parton density functions in RAPGAP for the data correction leads to an uncertainty of below 1%.

Fragmentation: The parameter of the Kartvelishvili fragmentation function in RAPGAP is varied in the range given in Table 1. The resulting differences in the cross section are between 1% and 5%.

Electron energy: The systematic uncertainty on the SpaCal energy scale is 0.5% which results in a systematic error of typically below 1%, but up to 10% at large D^* inelasticity z (see Sect. 6).

Table 7 Double differential D^* cross sections as a function of $\eta(D^*)$ and $p_T(D^*)$ and as a function of $\eta(D^*)$ and $p_T^*(D^*)$ in the kinematic range of $5 < Q^2 < 100 \text{ GeV}^2$, $0.02 < y < 0.7$, $|\eta(D^*)| < 1.8$, $p_T(D^*) > 1.25 \text{ GeV}$. The first quoted uncertainty is statistical and the second is systematic

η range		$d^2\sigma/d\eta dp_T$ [nb/GeV]			$d^2\sigma/d\eta dp_T^*$ [nb/GeV]		
		1.25 < p_T < 2.00 GeV			0.30 < p_T^* < 1.25 GeV		
-1.8	-1.2	0.760	± 0.074	$\pm_{0.055}^{0.058}$	0.547	± 0.051	$\pm_{0.041}^{0.041}$
-1.2	-0.6	0.701	± 0.055	$\pm_{0.052}^{0.052}$	0.453	± 0.035	$\pm_{0.037}^{0.037}$
-0.6	0.0	0.704	± 0.057	$\pm_{0.052}^{0.052}$	0.443	± 0.038	$\pm_{0.051}^{0.051}$
0.0	0.6	0.663	± 0.062	$\pm_{0.049}^{0.049}$	0.398	± 0.046	$\pm_{0.047}^{0.046}$
0.6	1.2	0.760	± 0.078	$\pm_{0.054}^{0.053}$	0.427	± 0.084	$\pm_{0.070}^{0.072}$
1.2	1.8	1.23	± 0.15	$\pm_{0.09}^{0.09}$	0.56	± 0.18	$\pm_{0.05}^{0.04}$
		2.00 < p_T < 2.75 GeV			1.25 < p_T^* < 2.00 GeV		
-1.8	-1.2	0.573	± 0.042	$\pm_{0.044}^{0.044}$	0.481	± 0.047	$\pm_{0.035}^{0.038}$
-1.2	-0.6	0.586	± 0.030	$\pm_{0.041}^{0.042}$	0.583	± 0.040	$\pm_{0.041}^{0.041}$
-0.6	0.0	0.688	± 0.034	$\pm_{0.051}^{0.051}$	0.640	± 0.044	$\pm_{0.045}^{0.047}$
0.0	0.6	0.703	± 0.043	$\pm_{0.050}^{0.050}$	0.614	± 0.060	$\pm_{0.048}^{0.043}$
0.6	1.2	0.783	± 0.045	$\pm_{0.055}^{0.055}$	0.708	± 0.079	$\pm_{0.057}^{0.051}$
1.2	1.8	0.723	± 0.062	$\pm_{0.052}^{0.051}$	0.77	± 0.16	$\pm_{0.06}^{0.06}$
		2.75 < p_T < 4.00 GeV			2.00 < p_T^* < 3.00 GeV		
-1.8	-1.2	0.227	± 0.017	$\pm_{0.017}^{0.018}$	0.336	± 0.028	$\pm_{0.029}^{0.029}$
-1.2	-0.6	0.336	± 0.014	$\pm_{0.023}^{0.023}$	0.390	± 0.021	$\pm_{0.027}^{0.029}$
-0.6	0.0	0.359	± 0.014	$\pm_{0.025}^{0.025}$	0.392	± 0.024	$\pm_{0.028}^{0.028}$
0.0	0.6	0.401	± 0.016	$\pm_{0.028}^{0.028}$	0.474	± 0.028	$\pm_{0.035}^{0.034}$
0.6	1.2	0.377	± 0.017	$\pm_{0.026}^{0.027}$	0.549	± 0.033	$\pm_{0.040}^{0.040}$
1.2	1.8	0.304	± 0.024	$\pm_{0.024}^{0.024}$	0.530	± 0.057	$\pm_{0.039}^{0.038}$
		4.00 < p_T < 6.00 GeV			3.00 < p_T^* < 6.00 GeV		
-1.8	-1.2	0.0368	± 0.0051	$\pm_{0.0034}^{0.0034}$	0.0419	± 0.0047	$\pm_{0.0040}^{0.0046}$
-1.2	-0.6	0.1017	± 0.0051	$\pm_{0.0074}^{0.0072}$	0.0875	± 0.0042	$\pm_{0.0068}^{0.0085}$
-0.6	0.0	0.1480	± 0.0059	$\pm_{0.0104}^{0.0104}$	0.1179	± 0.0048	$\pm_{0.0095}^{0.0099}$
0.0	0.6	0.1502	± 0.0068	$\pm_{0.0108}^{0.0107}$	0.1203	± 0.0055	$\pm_{0.0103}^{0.0106}$
0.6	1.2	0.1503	± 0.0068	$\pm_{0.0109}^{0.0106}$	0.1185	± 0.0063	$\pm_{0.0095}^{0.0103}$
1.2	1.8	0.0991	± 0.0095	$\pm_{0.0079}^{0.0075}$	0.0947	± 0.0095	$\pm_{0.0072}^{0.0077}$
		6.00 < p_T < 20.00 GeV			6.00 < p_T^* < 20.00 GeV		
-1.8	-1.2	0.00073	± 0.00030	$\pm_{0.00012}^{0.00009}$	0.00030	± 0.00027	$\pm_{0.00005}^{0.00004}$
-1.2	-0.6	0.00243	± 0.00035	$\pm_{0.00018}^{0.00018}$	0.00196	± 0.00028	$\pm_{0.00016}^{0.00021}$
-0.6	0.0	0.00653	± 0.00050	$\pm_{0.00050}^{0.00047}$	0.00377	± 0.00040	$\pm_{0.00029}^{0.00036}$
0.0	0.6	0.00761	± 0.00053	$\pm_{0.00057}^{0.00056}$	0.00439	± 0.00047	$\pm_{0.00044}^{0.00051}$
0.6	1.2	0.00724	± 0.00057	$\pm_{0.00064}^{0.00058}$	0.00571	± 0.00054	$\pm_{0.00051}^{0.00052}$
1.2	1.8	0.00462	± 0.00076	$\pm_{0.00082}^{0.00082}$	0.00257	± 0.00079	$\pm_{0.00021}^{0.00020}$

Electron angle: The angular resolution of the SpaCal/BPC of 0.5 mrad leads to a systematic uncertainty of typically 2%.

Hadronic energy: The systematic uncertainty on the energy scale of the hadronic final state is 2%. The influence in general is small (below 0.5%) but leads to larger uncer-

tainties of up to 20% at large D^* inelasticity $z(D^*)$ and small y .

All sources of the systematic errors are assumed to be uncorrelated between the sources and added in quadrature. This results in an overall systematic uncertainty of 7.6%.

Fig. 6 Double differential D^* cross section as a function of the transverse momentum $p_T(D^*)$ and pseudo-rapidity $\eta(D^*)$ in the laboratory frame. The measurements correspond to the kinematic range of $5 < Q^2 < 100 \text{ GeV}^2$, $0.02 < y < 0.7$ and $|\eta(D^*)| < 1.8$ and $p_T(D^*) > 1.25 \text{ GeV}$. The data are shown as *points*, the *inner error bars* show the statistical error, the *outer error bars* represent the statistical and systematic errors added in quadrature. The data are compared to predictions by the MC program RAPGAP with two different proton parton densities and by the MC program CASCADE

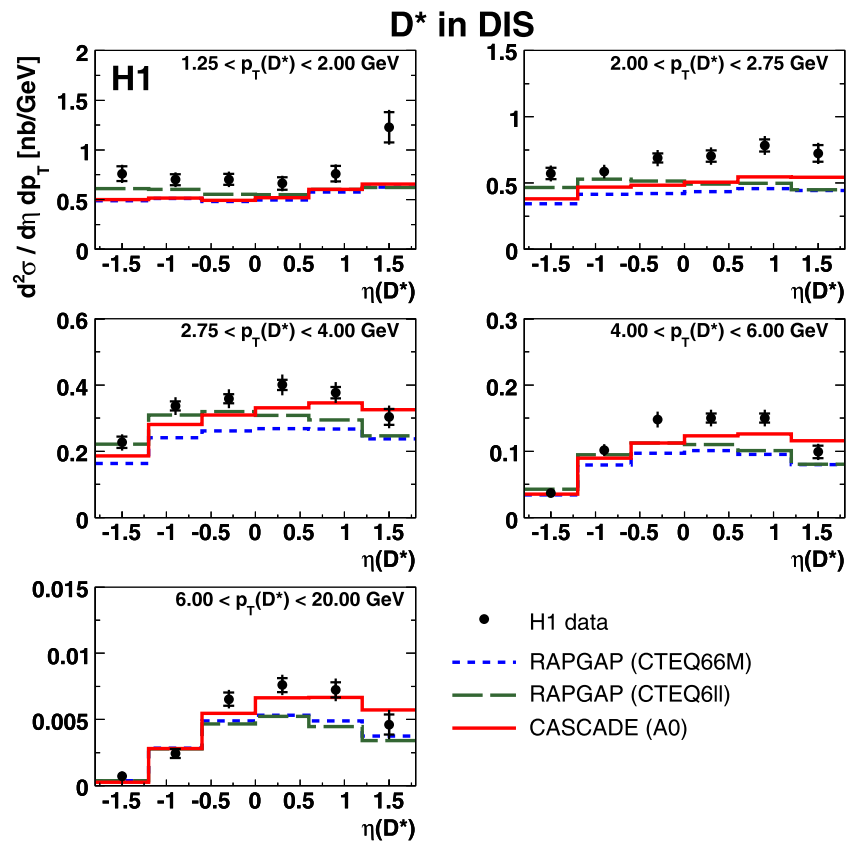


Fig. 7 Double differential D^* cross section as a function of the transverse momentum $p_T(D^*)$ and pseudo-rapidity $\eta(D^*)$ in the laboratory frame. The measurements correspond to the kinematic range of $5 < Q^2 < 100 \text{ GeV}^2$, $0.02 < y < 0.7$ and $|\eta(D^*)| < 1.8$ and $p_T(D^*) > 1.25 \text{ GeV}$. The data are shown as *points*, the *inner error bars* show the statistical error, the *outer error bars* represent the statistical and systematic errors added in quadrature. The data are compared to predictions by the next-to-leading order calculation HVQDIS with two different proton parton densities. The *bands* indicate the theoretical uncertainties (Table 2)

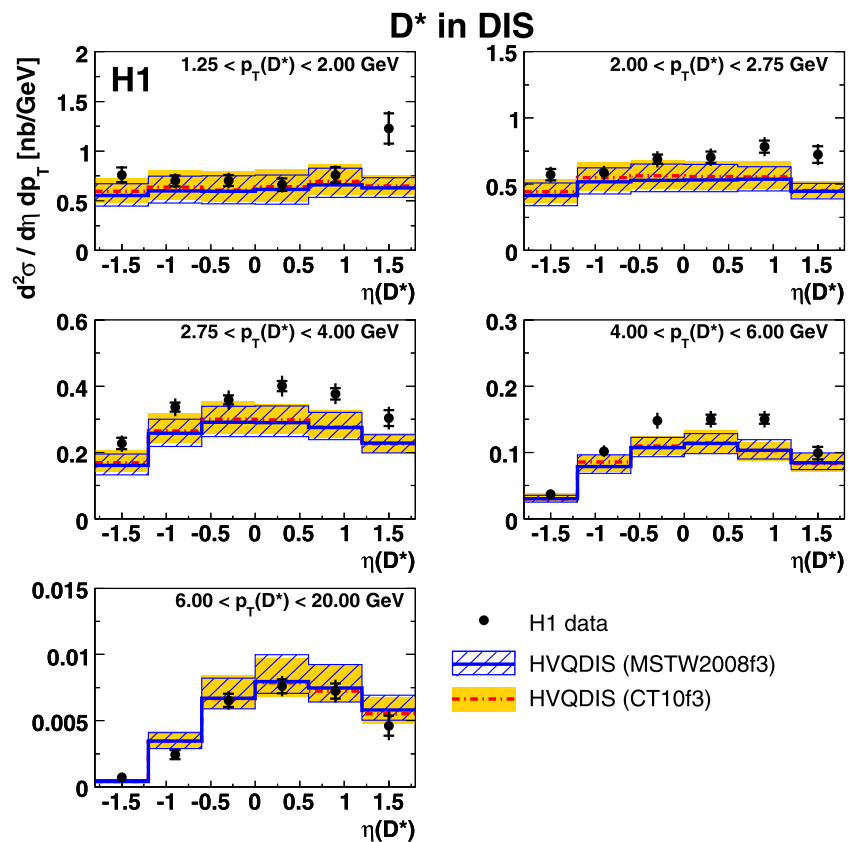


Fig. 8 Double differential D^* cross section as a function of the transverse momentum in the γp centre-of-mass frame $p_T^*(D^*)$ and the pseudo-rapidity $\eta(D^*)$ in the laboratory frame. The measurements correspond to the kinematic range of $5 < Q^2 < 100 \text{ GeV}^2$, $0.02 < y < 0.7$ and $|\eta(D^*)| < 1.8$ and $p_T(D^*) > 1.25 \text{ GeV}$. The data are shown as *points*, the *inner error bars* show the statistical error, the *outer error bars* represent the statistical and systematic errors added in quadrature. The data are compared to predictions by the MC program RAPGAP with two different proton parton densities and by the MC program CASCADE

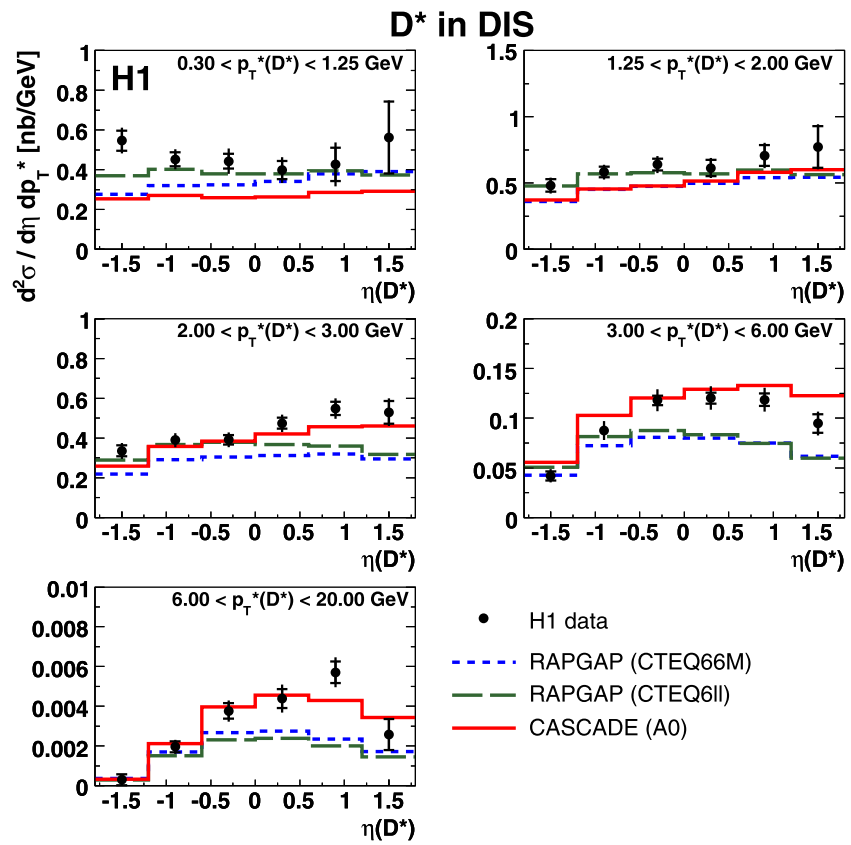


Fig. 9 Double differential D^* cross section as a function of the transverse momentum in the γp centre-of-mass frame $p_T^*(D^*)$ and the pseudo-rapidity $\eta(D^*)$ in the laboratory frame. The measurements correspond to the kinematic range of $5 < Q^2 < 100 \text{ GeV}^2$, $0.02 < y < 0.7$ and $|\eta(D^*)| < 1.8$ and $p_T(D^*) > 1.25 \text{ GeV}$. The data are shown as *points*, the *inner error bars* show the statistical error, the *outer error bars* represent the statistical and systematic errors added in quadrature. The data are compared to predictions by the next-to-leading order calculation HVQDIS with two different proton parton densities. The *bands* indicate the theoretical uncertainties (Table 2)

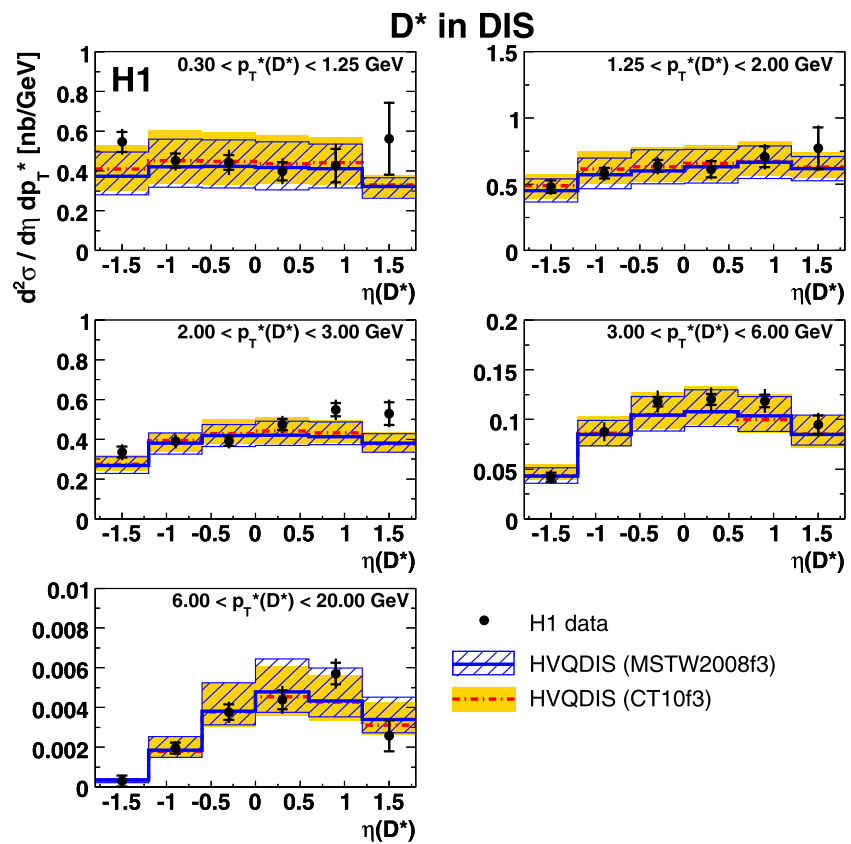


Table 8 Double differential D^* cross sections as a function of y and Q^2 in two different kinematic ranges: $|\eta(D^*)| < 1.8$ and $p_T(D^*) > 1.25$ GeV or $|\eta(D^*)| < 1.5$ and $p_T(D^*) > 1.5$ GeV. The first quoted uncertainty is statistical and the second is systematic

y range		$d^2\sigma/dy dQ^2$ [nb/GeV ²] for $p_T(D^*) > 1.25$ GeV, $ \eta(D^*) < 1.8$			$d^2\sigma/dy dQ^2$ [nb/GeV ²] for $p_T(D^*) > 1.5$ GeV, $ \eta(D^*) < 1.5$		
$5 < Q^2 < 9$ GeV ²							
0.02	0.05	2.27	± 0.19	$\pm_{-0.24}^{0.22}$	1.23	± 0.14	$\pm_{-0.11}^{0.11}$
0.05	0.09	1.95	± 0.16	$\pm_{-0.14}^{0.14}$	1.57	± 0.12	$\pm_{-0.14}^{0.12}$
0.09	0.16	1.767	± 0.096	$\pm_{-0.127}^{0.127}$	1.378	± 0.077	$\pm_{-0.131}^{0.114}$
0.16	0.32	0.954	± 0.052	$\pm_{-0.072}^{0.077}$	0.839	± 0.039	$\pm_{-0.080}^{0.077}$
0.32	0.70	0.361	± 0.024	$\pm_{-0.027}^{0.030}$	0.243	± 0.018	$\pm_{-0.025}^{0.024}$
$9 < Q^2 < 14$ GeV ²							
0.02	0.05	0.845	± 0.101	$\pm_{-0.086}^{0.078}$	0.457	± 0.082	$\pm_{-0.042}^{0.045}$
0.05	0.09	0.953	± 0.085	$\pm_{-0.075}^{0.072}$	0.745	± 0.068	$\pm_{-0.074}^{0.065}$
0.09	0.16	0.687	± 0.054	$\pm_{-0.051}^{0.050}$	0.581	± 0.044	$\pm_{-0.052}^{0.048}$
0.16	0.32	0.447	± 0.029	$\pm_{-0.031}^{0.032}$	0.414	± 0.028	$\pm_{-0.035}^{0.031}$
0.32	0.70	0.193	± 0.015	$\pm_{-0.015}^{0.015}$	0.144	± 0.011	$\pm_{-0.013}^{0.013}$
$14 < Q^2 < 23$ GeV ²							
0.02	0.05	0.444	± 0.055	$\pm_{-0.049}^{0.052}$	0.249	± 0.032	$\pm_{-0.023}^{0.022}$
0.05	0.09	0.434	± 0.040	$\pm_{-0.033}^{0.030}$	0.359	± 0.035	$\pm_{-0.033}^{0.030}$
0.09	0.16	0.356	± 0.028	$\pm_{-0.029}^{0.030}$	0.303	± 0.021	$\pm_{-0.032}^{0.030}$
0.16	0.32	0.249	± 0.015	$\pm_{-0.018}^{0.018}$	0.208	± 0.012	$\pm_{-0.019}^{0.016}$
0.32	0.70	0.0887	± 0.0078	$\pm_{-0.0077}^{0.0079}$	0.0659	± 0.0055	$\pm_{-0.0068}^{0.0065}$
$23 < Q^2 < 45$ GeV ²							
0.02	0.05	0.105	± 0.016	$\pm_{-0.011}^{0.012}$	0.087	± 0.012	$\pm_{-0.014}^{0.014}$
0.05	0.09	0.160	± 0.016	$\pm_{-0.014}^{0.013}$	0.120	± 0.013	$\pm_{-0.012}^{0.011}$
0.09	0.16	0.125	± 0.011	$\pm_{-0.009}^{0.010}$	0.1211	± 0.0095	$\pm_{-0.0120}^{0.0107}$
0.16	0.32	0.0885	± 0.0059	$\pm_{-0.0064}^{0.0062}$	0.0744	± 0.0046	$\pm_{-0.0065}^{0.0056}$
0.32	0.70	0.0375	± 0.0031	$\pm_{-0.0030}^{0.0031}$	0.0304	± 0.0024	$\pm_{-0.0029}^{0.0027}$
$45 < Q^2 < 100$ GeV ²							
0.02	0.05	0.0150	± 0.0085	$\pm_{-0.0020}^{0.0015}$	0.0054	± 0.0026	$\pm_{-0.0005}^{0.0007}$
0.05	0.09	0.0302	± 0.0054	$\pm_{-0.0024}^{0.0024}$	0.0249	± 0.0041	$\pm_{-0.0025}^{0.0022}$
0.09	0.16	0.0258	± 0.0034	$\pm_{-0.0020}^{0.0021}$	0.0215	± 0.0028	$\pm_{-0.0023}^{0.0023}$
0.16	0.32	0.0235	± 0.0022	$\pm_{-0.0018}^{0.0019}$	0.0236	± 0.0019	$\pm_{-0.0024}^{0.0022}$
0.32	0.70	0.0097	± 0.0011	$\pm_{-0.0008}^{0.0008}$	0.00729	± 0.00085	$\pm_{-0.00072}^{0.00065}$

6 Cross sections

The cross section in the visible range defined in Table 3 is measured to be:

$$\sigma_{\text{vis}}(ep \rightarrow eD^{*\pm}X) = 6.44 \pm 0.09 \text{ (stat.)} \pm 0.49 \text{ (syst.) nb.} \tag{2}$$

The corresponding predictions from RAPGAP (CTEQ6LL), RAPGAP (CTEQ6.6M), and CASCADE (A0) amount to 5.02 nb, 4.37 nb, and 5.09 nb, respectively. The NLO calculation HVQDIS yields $5.98_{-0.88}^{+1.10}$ nb with CT10f3 as the

proton PDF and $5.52_{-0.82}^{+0.94}$ nb with MSTW2008f3, where the uncertainty is determined by varying the parameters according to Table 2 and adding the resulting uncertainties in quadrature. The HVQDIS predictions are slightly below the measurement but agree with the data within errors.

In Table 5 and Figs. 2 and 3 the single differential cross sections are presented as a function of variables describing the event kinematics: the photon virtuality Q^2 , the inelasticity y and Bjorken x . The measurements are compared to the predictions of the MC programs RAPGAP and CASCADE (Fig. 2) and of the next-to-leading order calculation with the HVQDIS program (Fig. 3). Since the theoretical calcula-

Fig. 10 Double differential D^* cross section as a function of the photon virtuality Q^2 and the inelasticity y . The measurements correspond to the kinematic range of $5 < Q^2 < 100 \text{ GeV}^2$, $0.02 < y < 0.7$ and $|\eta(D^*)| < 1.8$ and $p_T(D^*) > 1.25 \text{ GeV}$. The data are shown as *points*, the *inner error bars* show the statistical error, the *outer error bars* represent the statistical and systematic errors added in quadrature. The data are compared to predictions by the MC program RAPGAP with two different proton parton densities and by the MC program CASCADE

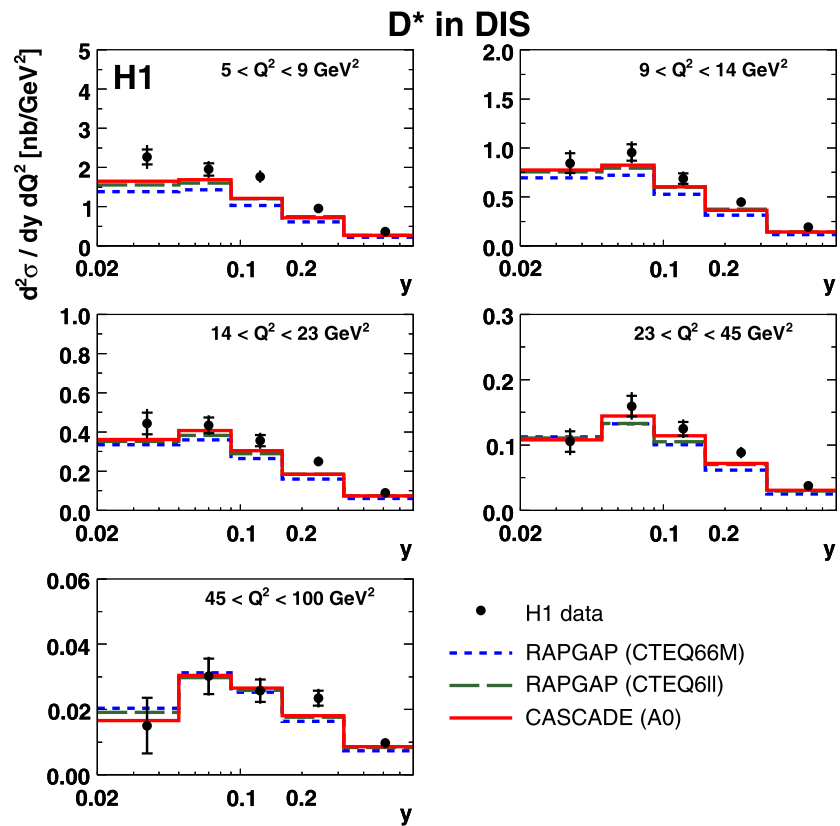
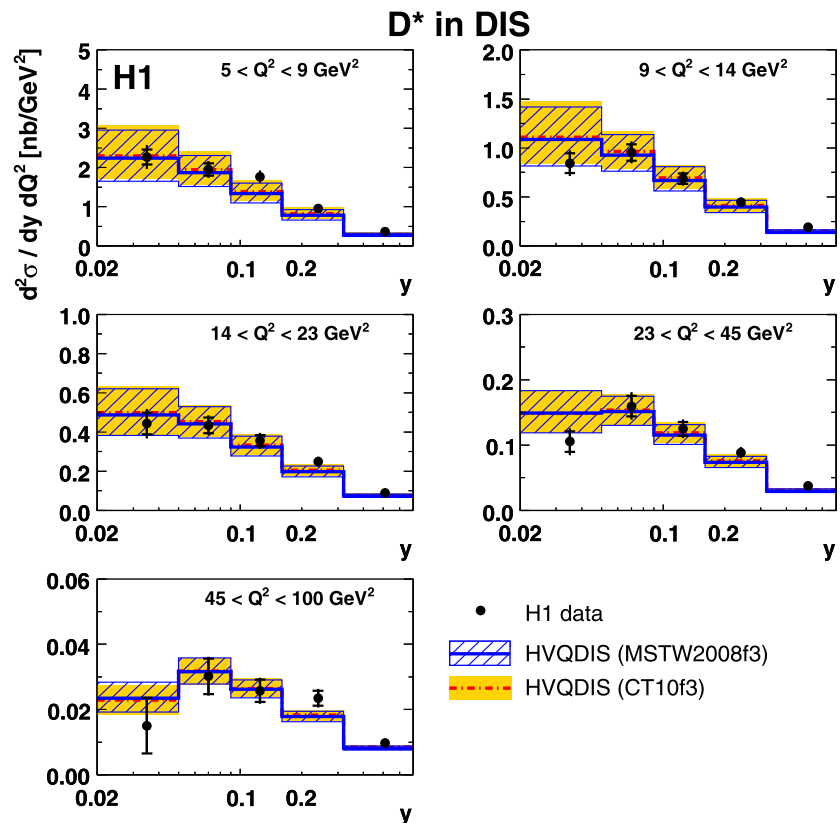


Fig. 11 Double differential D^* cross section as a function of photon virtuality Q^2 and the inelasticity y . The measurements correspond to the kinematic range of $5 < Q^2 < 100 \text{ GeV}^2$, $0.02 < y < 0.7$ and $|\eta(D^*)| < 1.8$ and $p_T(D^*) > 1.25 \text{ GeV}$. The data are shown as *points*, the *inner error bars* show the statistical error, the *outer error bars* represent the statistical and systematic errors added in quadrature. The data are compared to predictions by the next-to-leading order calculation HVQDIS with two different proton parton densities. The *bands* indicate the theoretical uncertainties (Table 2)



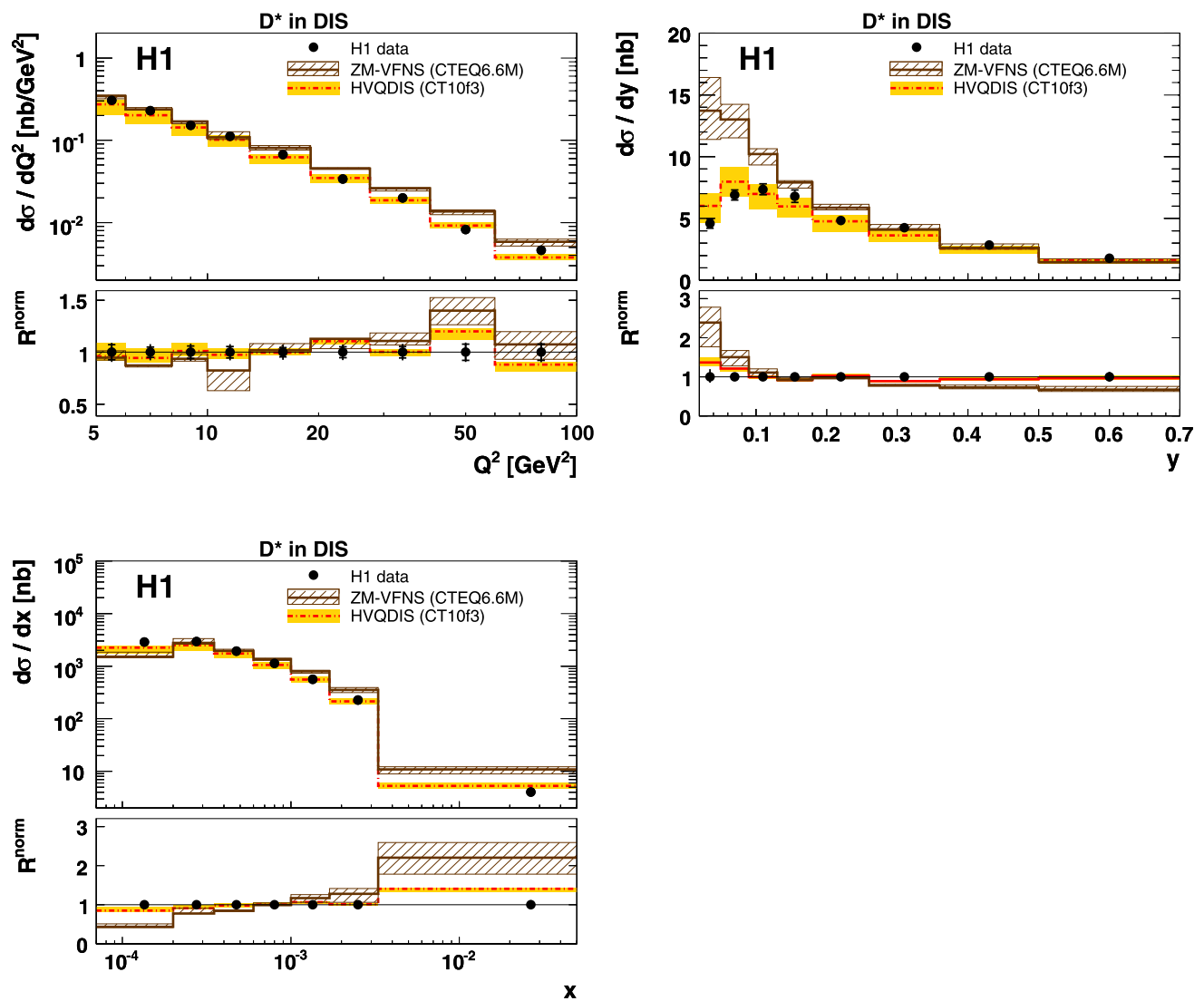


Fig. 12 Differential D^* cross section as a function of photon virtuality Q^2 , the inelasticity y and Bjorken x . The measurements correspond to the kinematic range of $5 < Q^2 < 100 \text{ GeV}^2$, $0.02 < y < 0.7$, $|\eta(D^*)| < 1.8$, $p_T(D^*) > 1.25 \text{ GeV}$ with an additional cut on the D^* transverse momentum in the γp centre-of-mass frame $p_T^*(D^*) >$

2.0 GeV . The data are shown as *points*, the *inner error bars* show the statistical error, the *outer error bars* represent the statistical and systematic errors added in quadrature. The data are compared to a prediction to next-to-leading order in the ZM-VFNS and to HVQDIS. The *bands* indicate the theoretical uncertainties (Table 2)

tions predict smaller cross sections than the measurement, the normalised ratio R^{norm} of theory to data is shown in the lower part of the figures, which facilitates the shape comparison between the different theoretical predictions and the data. This ratio is defined as:

$$R^{\text{norm}} = \frac{1/\sigma_{\text{vis}}^{\text{theo}} \cdot \frac{d\sigma^{\text{theo}}}{dY}}{1/\sigma_{\text{vis}}^{\text{data}} \cdot \frac{d\sigma^{\text{data}}}{dY}}, \tag{3}$$

where $\sigma_{\text{vis}}^{\text{theo}}$ and $d\sigma^{\text{theo}}/dY$ are the total and differential cross section of the model under consideration and Y denotes any measured variable. The normalisation uncertainties of the data (luminosity, branching ratio and half of the

tracking uncertainty) cancel in this ratio. Similarly, uncertainty sources of the NLO predictions altering only the normalisation do not affect R^{norm} since for each variation the total and the differential cross section are varied simultaneously. In all predictions the decrease with Q^2 is slightly less steep than in data. The y dependence is reasonably well described by all predictions. The dependence on x is slightly less steep in all predictions than in the data, an effect which is larger for the NLO calculations.

In Table 6 and Figs. 4 and 5 the single differential cross sections are presented as a function of the kinematic variables of the D^* meson: the transverse momentum $p_T(D^*)$ and pseudo-rapidity $\eta(D^*)$ in the laboratory frame, the

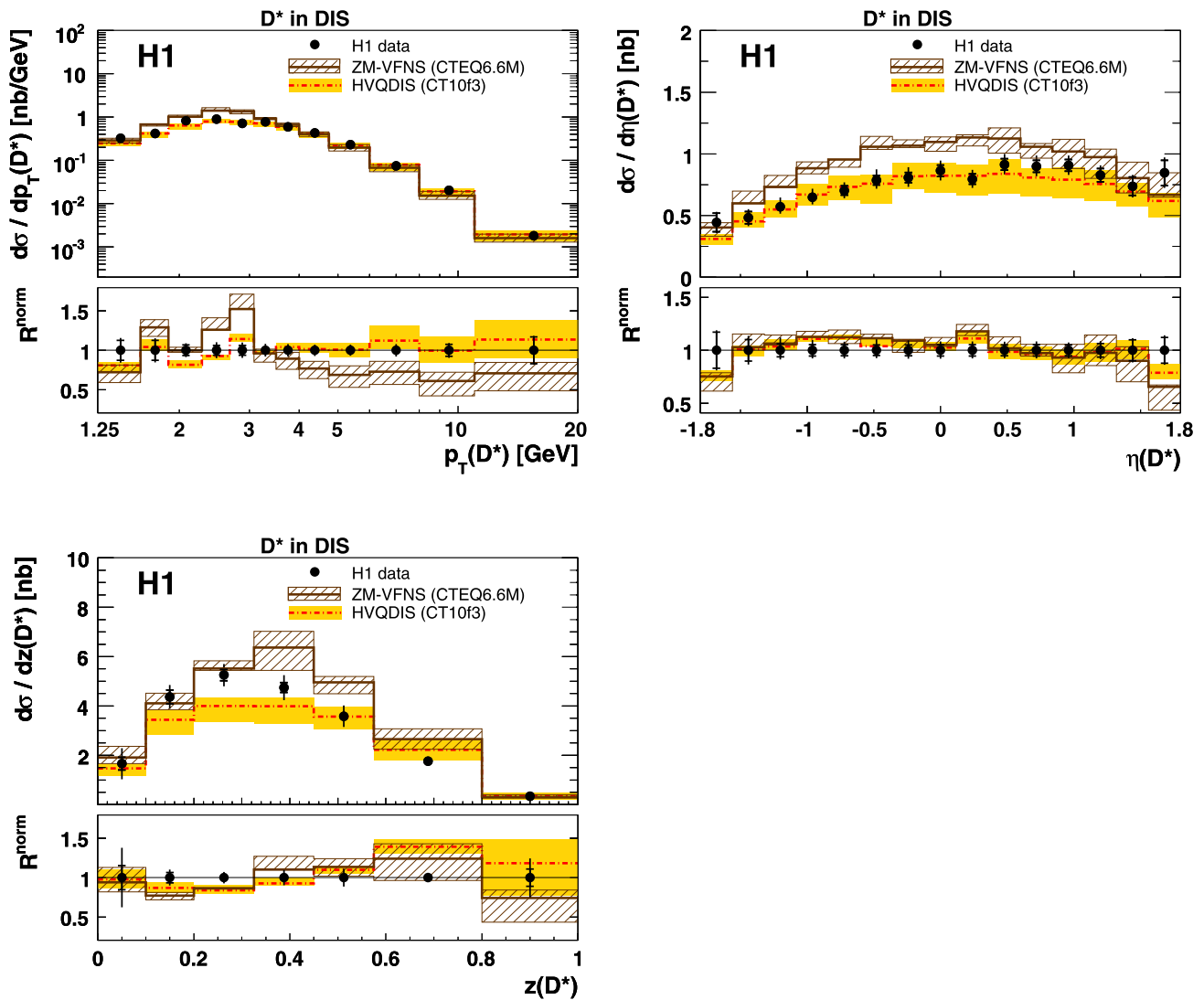


Fig. 13 Differential D^* cross section as a function of the transverse momentum $p_T(D^*)$ and pseudo-rapidity $\eta(D^*)$ in the laboratory frame and the D^* inelasticity $z(D^*)$. The measurements correspond to the kinematic range of $5 < Q^2 < 100 \text{ GeV}^2$, $0.02 < y < 0.7$, $|\eta(D^*)| < 1.8$, $p_T(D^*) > 1.25 \text{ GeV}$ with an additional cut on the D^* transverse momentum in the γp centre-of-mass frame $p_T^*(D^*) >$

2.0 GeV . The data are shown as *points*, the *inner error bars* show the statistical error, the *outer error bars* represent the statistical and systematic errors added in quadrature. The data are compared to a prediction to next-to-leading order in the ZM-VFNS and to HVQDIS. The *bands* indicate the theoretical uncertainties (Table 2)

transverse momentum $p_T^*(D^*)$ in the γp centre-of-mass frame and the D^* inelasticity $z(D^*)$. The D^* inelasticity $z(D^*)$ corresponds to the fraction of the virtual photon momentum carried by the D^* meson and is determined as $z(D^*) = (P \cdot p_{D^*}) / (P \cdot q) = (E - p_z)_{D^*} / 2yE_e$ where E_e is the energy of the incoming electron and P , q and p_{D^*} denote the four-momenta of the incoming proton, the exchanged photon and the D^* meson, respectively. All predictions are able to describe the shape of the $p_T(D^*)$ distribution of the data reasonably well, although RAPGAP has a tendency to underestimate the data at large $p_T(D^*)$. The shape of the η distribution shows sensitivity to the use of different parton densities in the RAPGAP MC. The predic-

tion based on CTEQ6.6M agrees better with the data than the prediction based on CTEQ6LL. A very good description of the η shape is obtained with the CASCADE MC. The HVQDIS calculations with CT10f3 and MSTW2008f3 both describe the η distribution reasonably well, but have a tendency to be too low in the positive η (forward) region. For the transverse momentum $p_T^*(D^*)$ in the γp centre-of-mass frame, the RAPGAP MC using either PDF is too steep at large $p_T^*(D^*)$, while the CASCADE prediction generally has a different shape. The NLO predictions are in good agreement with the data. The $z(D^*)$ dependence is not described by any of the calculations, showing a deficit of all predictions at low $z(D^*)$ values.

In order to investigate the correlation between pseudo-rapidity and transverse momentum, a double differential measurement in $p_T(D^*)$ and $\eta(D^*)$ is performed. In Table 7 and Figs. 6 and 7 the double differential cross section is presented as a function of the pseudo-rapidity $\eta(D^*)$ in bins of the transverse momentum of the D^* meson $p_T(D^*)$. In the backward direction almost no D^* mesons with large trans-

Table 9 Differential D^* cross section as a function of Q^2 , y and x in the kinematic range of $5 < Q^2 < 100 \text{ GeV}^2$, $0.02 < y < 0.7$, $|\eta(D^*)| < 1.5$ and $p_T(D^*) > 1.5 \text{ GeV}$. The first quoted uncertainty is statistical and the second is systematic

Q^2 range [GeV ²]		$d\sigma/dQ^2$ [nb/GeV ²]		
5.0	6.0	0.552	± 0.032	$\pm_{0.043}^{0.046}$
6.0	8.0	0.398	± 0.016	$\pm_{0.030}^{0.031}$
8.0	10.0	0.278	± 0.013	$\pm_{0.020}^{0.020}$
10.0	13.0	0.1983	± 0.0088	$\pm_{0.0143}^{0.0143}$
13.0	19.0	0.1236	± 0.0042	$\pm_{0.0088}^{0.0088}$
19.0	27.5	0.0679	± 0.0028	$\pm_{0.0048}^{0.0048}$
27.5	40.0	0.0374	± 0.0017	$\pm_{0.0027}^{0.0027}$
40.0	60.0	0.01562	± 0.00095	$\pm_{0.00110}^{0.00113}$
60.0	100.0	0.00724	± 0.00045	$\pm_{0.00051}^{0.00053}$

y range		$d\sigma/dy$ [nb]		
0.02	0.05	12.21	± 0.64	$\pm_{1.47}^{1.47}$
0.05	0.09	16.39	± 0.69	$\pm_{1.20}^{1.21}$
0.09	0.13	15.89	± 0.72	$\pm_{1.25}^{1.30}$
0.13	0.18	12.71	± 0.61	$\pm_{0.92}^{0.92}$
0.18	0.26	10.90	± 0.42	$\pm_{0.82}^{0.84}$
0.26	0.36	6.85	± 0.31	$\pm_{0.51}^{0.53}$
0.36	0.50	4.24	± 0.22	$\pm_{0.34}^{0.37}$
0.50	0.70	2.13	± 0.17	$\pm_{0.18}^{0.20}$

x range		$d\sigma/dx$ [nb]		
0.00007	0.00020	3320	± 200	\pm_{250}^{270}
0.00020	0.00035	4780	± 220	\pm_{350}^{370}
0.00035	0.00060	3430	± 130	\pm_{250}^{250}
0.00060	0.00100	2034	± 81	\pm_{145}^{147}
0.00100	0.00170	1225	± 46	\pm_{89}^{90}
0.00170	0.00330	446	± 18	\pm_{34}^{34}
0.00330	0.05000	10.15	± 0.44	$\pm_{0.82}^{0.84}$

Table 10 Differential D^* cross section as a function of $p_T(D^*)$, $\eta(D^*)$, $p_T^*(D^*)$ and $z(D^*)$ in the kinematic range of $5 < Q^2 < 100 \text{ GeV}^2$, $0.02 < y < 0.7$, $|\eta(D^*)| < 1.5$ and $p_T(D^*) > 1.5 \text{ GeV}$. The first quoted uncertainty is statistical and the second is systematic

p_T range [GeV]		$d\sigma/dp_T$ [nb/GeV]		
1.50	1.88	2.34	± 0.15	$\pm_{0.17}^{0.17}$
1.88	2.28	2.042	± 0.093	$\pm_{0.144}^{0.144}$
2.28	2.68	1.959	± 0.070	$\pm_{0.140}^{0.140}$
2.68	3.08	1.384	± 0.050	$\pm_{0.096}^{0.096}$
3.08	3.50	1.152	± 0.043	$\pm_{0.079}^{0.080}$
3.50	4.00	0.814	± 0.028	$\pm_{0.056}^{0.056}$
4.00	4.75	0.575	± 0.018	$\pm_{0.040}^{0.040}$
4.75	6.00	0.2714	± 0.0088	$\pm_{0.0187}^{0.0189}$
6.00	8.00	0.0851	± 0.0037	$\pm_{0.0058}^{0.0058}$
8.00	11.00	0.0211	± 0.0015	$\pm_{0.0016}^{0.0017}$
11.00	20.00	0.00178	± 0.00028	$\pm_{0.00012}^{0.00013}$

η range		$d\sigma/d\eta$ [nb]		
-1.50	-1.25	1.229	± 0.077	$\pm_{0.088}^{0.090}$
-1.25	-1.00	1.319	± 0.062	$\pm_{0.094}^{0.098}$
-1.00	-0.75	1.501	± 0.061	$\pm_{0.108}^{0.113}$
-0.75	-0.50	1.635	± 0.065	$\pm_{0.116}^{0.118}$
-0.50	-0.25	1.569	± 0.063	$\pm_{0.109}^{0.112}$
-0.25	0.00	1.629	± 0.066	$\pm_{0.116}^{0.118}$
0.00	0.25	1.667	± 0.070	$\pm_{0.117}^{0.117}$
0.25	0.50	1.677	± 0.074	$\pm_{0.119}^{0.121}$
0.50	0.75	1.756	± 0.078	$\pm_{0.124}^{0.126}$
0.75	1.00	1.746	± 0.080	$\pm_{0.128}^{0.131}$
1.00	1.25	2.024	± 0.095	$\pm_{0.146}^{0.150}$
1.25	1.50	1.73	± 0.12	$\pm_{0.12}^{0.13}$

p_T^* range [GeV]		$d\sigma/dp_T^*$ [nb/GeV]		
0.300	0.700	0.75	± 0.13	$\pm_{0.13}^{0.13}$
0.700	1.125	1.34	± 0.12	$\pm_{0.14}^{0.14}$
1.125	1.500	1.48	± 0.13	$\pm_{0.16}^{0.16}$
1.500	1.880	1.62	± 0.12	$\pm_{0.12}^{0.11}$
1.880	2.280	1.511	± 0.093	$\pm_{0.108}^{0.106}$
2.280	2.680	1.163	± 0.073	$\pm_{0.086}^{0.087}$
2.680	3.080	0.884	± 0.055	$\pm_{0.061}^{0.061}$
3.080	3.500	0.570	± 0.039	$\pm_{0.040}^{0.041}$
3.500	4.250	0.403	± 0.020	$\pm_{0.030}^{0.030}$
4.250	6.000	0.1785	± 0.0069	$\pm_{0.0156}^{0.0166}$
6.000	11.000	0.0269	± 0.0015	$\pm_{0.0025}^{0.0026}$
11.000	20.000	0.00186	± 0.00041	$\pm_{0.00016}^{0.00020}$

z range		$d\sigma/dz$ [nb]		
0.000	0.100	3.29	± 0.41	$\pm_{0.29}^{0.29}$
0.100	0.200	7.02	± 0.44	$\pm_{0.58}^{0.58}$
0.200	0.325	8.22	± 0.36	$\pm_{0.70}^{0.70}$
0.325	0.450	7.59	± 0.31	$\pm_{0.63}^{0.65}$
0.450	0.575	7.40	± 0.28	$\pm_{0.59}^{0.59}$
0.575	0.800	4.06	± 0.13	$\pm_{0.35}^{0.34}$
0.800	1.000	0.861	± 0.064	$\pm_{0.204}^{0.233}$

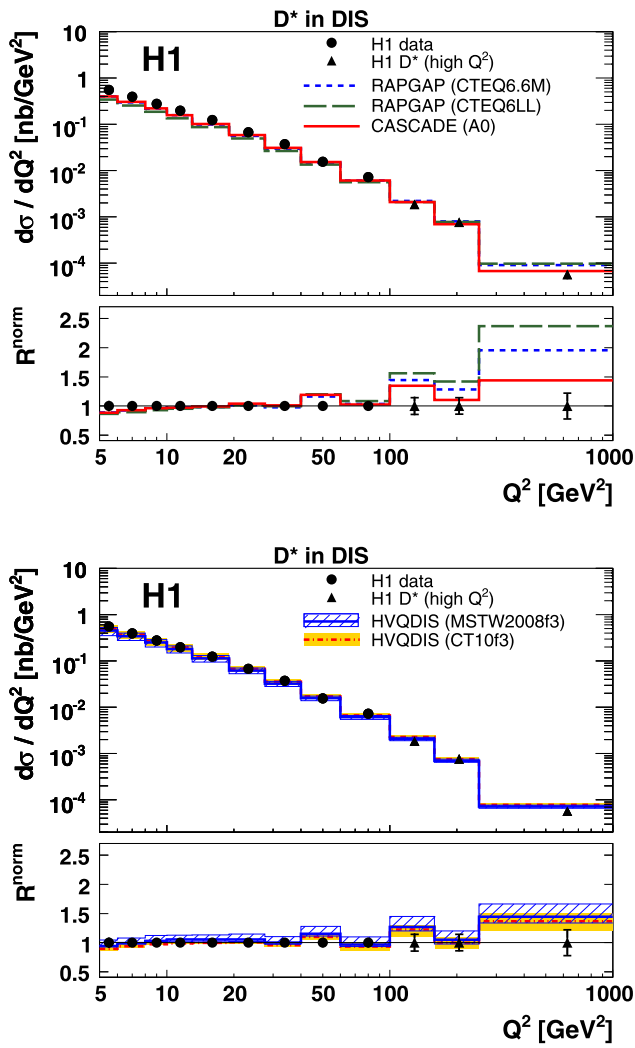


Fig. 14 Differential D^* cross section as a function of the photon virtuality Q^2 . The measurements correspond to the kinematic range of $0.02 < y < 0.7$, $|\eta(D^*)| < 1.5$ and $p_T(D^*) > 1.5$ GeV. The data of this measurement (points) are shown in a phase space with stronger restrictions on $\eta(D^*)$ and $p_T(D^*)$ to be comparable to a previous measurement at higher Q^2 [15] (triangles). The inner error bars show the statistical error, the outer error bars represent the statistical and systematic errors added in quadrature. The data are compared to predictions by the MC program RAPGAP with two different proton PDFs and by the MC program CASCADE (left) and to predictions by the next-to-leading order calculation HVQDIS with two different proton PDFs (right)

verse momentum are produced. At low transverse momenta all predictions are below the data in the very forward direction. At $p_T(D^*) > 6$ GeV the CASCADE and HVQDIS predictions give a good description of the data, while RAPGAP is too low.

While the transverse momentum of the D^* meson in the laboratory frame is correlated with the photon virtuality Q^2 , the transverse momentum in the γp centre-of-mass frame $p_T^*(D^*)$ is directly related to the hard subprocess. The double differential cross section as a function of $\eta(D^*)$ and

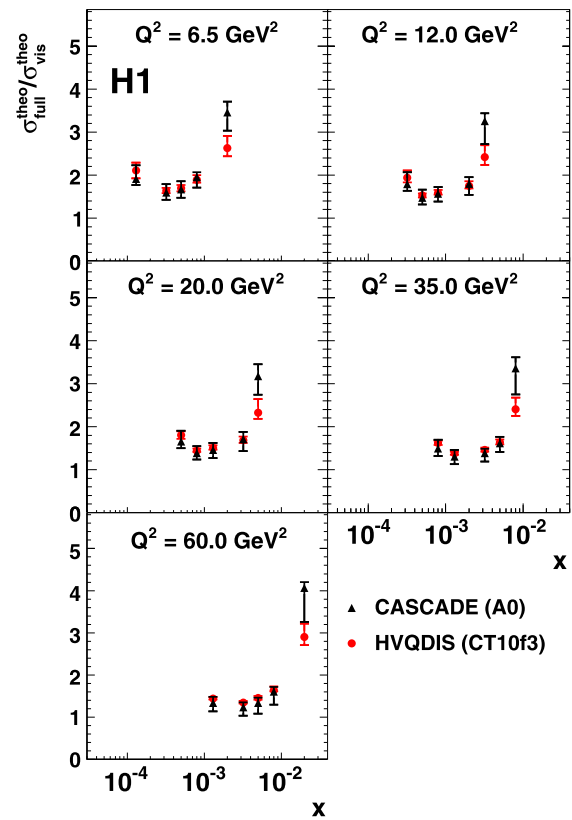


Fig. 15 Extrapolation factors from the visible phase space (Table 3) to the total phase space for the D^* meson as determined from HVQDIS and CASCADE. The error bars show the extrapolation uncertainty which is determined by varying the theory parameters listed in Table 2 for HVQDIS and in Table 1 for CASCADE

$p_T^*(D^*)$ are presented in Table 7 and Figs. 8 and 9. The distribution shows similar behaviour to the double differential cross section as a function of $\eta(D^*)$ and the transverse momentum $p_T(D^*)$ in the laboratory frame. They are in general better described by the predictions of CASCADE and HVQDIS, while RAPGAP underestimates the data for positive $\eta(D^*)$ at large $p_T^*(D^*)$.

The double differential cross section measurements in y and Q^2 are presented in Table 8 and Figs. 10 and 11. All predictions are able to describe the distribution reasonably well, independent of the PDF choice. At low Q^2 RAPGAP as well as CASCADE has a tendency to be lower than the data.

To allow a comparison to the ZM-VFNS predictions, the cross sections are also measured with an additional cut $p_T^*(D^*) > 2$ GeV. The measurements are shown in Tables 5 and 6 and in Figs. 12 and 13. The ZM-VFNS calculation overshoots the data at low y . The x dependence is less steep than for the data, and it has a different shape in $p_T(D^*)$. The dependence of the cross section on the other variables is described reasonably well. In general the ZM-VFNS prediction describes the data worse than the NLO FFNS cal-

Table 11 $F_2^{c\bar{c}}$ in bins of Q^2 and x extracted from measured D^* cross sections with two different programs, HVQDIS and CASCADE. The extrapolation uncertainty δ_{ext} is determined by varying model parameters within a program. The statistical (δ_{stat}) and systematic (δ_{syst}) uncertainties arise from the determination of the D^* cross section and are the same for both programs

Q^2 [GeV ²]	x	HVQDIS		δ_{stat} [%]	δ_{syst} [%]	CASCADE	
		$F_2^{c\bar{c}}$	δ_{ext} [%]			$F_2^{c\bar{c}}$	δ_{ext} [%]
6.5	1.3×10^{-4}	0.2160	$\pm_{8.7}^{8.5}$	± 6.7	$\pm_{8.1}^{7.7}$	0.2005	$\pm_{7.3}^{16.6}$
6.5	3.2×10^{-4}	0.1576	$\pm_{3.2}^{4.3}$	± 5.5	$\pm_{8.0}^{7.7}$	0.1634	$\pm_{10.7}^{12.3}$
6.5	5.0×10^{-4}	0.1516	$\pm_{4.5}^{4.2}$	± 5.4	$\pm_{7.3}^{7.2}$	0.1597	$\pm_{11.9}^{11.1}$
6.5	8.0×10^{-4}	0.1036	$\pm_{3.4}^{5.7}$	± 8.1	$\pm_{7.2}^{7.2}$	0.1153	$\pm_{12.6}^{6.0}$
6.5	2.0×10^{-3}	0.0735	$\pm_{7.2}^{10.8}$	± 8.6	$\pm_{10.4}^{9.9}$	0.1044	$\pm_{12.2}^{7.2}$
12.0	3.2×10^{-4}	0.2829	$\pm_{5.6}^{8.7}$	± 7.7	$\pm_{7.9}^{7.6}$	0.2727	$\pm_{8.6}^{15.5}$
12.0	5.0×10^{-4}	0.2123	$\pm_{2.9}^{3.1}$	± 6.6	$\pm_{7.1}^{7.1}$	0.2169	$\pm_{10.7}^{12.5}$
12.0	8.0×10^{-4}	0.1689	$\pm_{2.3}^{4.6}$	± 7.8	$\pm_{7.3}^{7.4}$	0.1779	$\pm_{11.7}^{10.0}$
12.0	2.0×10^{-3}	0.1226	$\pm_{3.5}^{6.1}$	± 8.9	$\pm_{7.7}^{7.7}$	0.1353	$\pm_{14.4}^{8.7}$
12.0	3.2×10^{-3}	0.0773	$\pm_{7.4}^{11.6}$	± 12.0	$\pm_{9.8}^{9.6}$	0.1125	$\pm_{16.5}^{5.7}$
18.0	5.0×10^{-4}	0.3221	$\pm_{5.0}^{4.6}$	± 8.8	$\pm_{9.1}^{8.5}$	0.3045	$\pm_{9.2}^{15.2}$
18.0	8.0×10^{-4}	0.2899	$\pm_{2.1}^{3.8}$	± 6.1	$\pm_{7.2}^{7.3}$	0.2964	$\pm_{10.6}^{11.7}$
18.0	1.3×10^{-3}	0.2167	$\pm_{2.9}^{4.0}$	± 8.0	$\pm_{8.3}^{8.2}$	0.2202	$\pm_{12.9}^{11.0}$
18.0	3.2×10^{-3}	0.1368	$\pm_{3.5}^{5.3}$	± 9.3	$\pm_{7.2}^{7.4}$	0.1471	$\pm_{16.0}^{10.1}$
18.0	5.0×10^{-3}	0.1033	$\pm_{6.0}^{13.6}$	± 12.5	$\pm_{11.5}^{11.3}$	0.1455	$\pm_{13.6}^{8.7}$
35.0	8.0×10^{-4}	0.3958	$\pm_{3.0}^{3.6}$	± 8.3	$\pm_{8.2}^{8.0}$	0.3620	$\pm_{11.7}^{14.0}$
35.0	1.3×10^{-3}	0.3188	$\pm_{2.4}^{2.8}$	± 6.7	$\pm_{7.1}^{7.2}$	0.3092	$\pm_{13.5}^{11.9}$
35.0	3.2×10^{-3}	0.2015	$\pm_{2.4}^{3.7}$	± 8.5	$\pm_{7.6}^{7.6}$	0.2000	$\pm_{14.2}^{7.5}$
35.0	5.0×10^{-3}	0.1616	$\pm_{2.7}^{4.2}$	± 9.9	$\pm_{8.7}^{8.3}$	0.1684	$\pm_{12.5}^{9.0}$
35.0	8.0×10^{-3}	0.0854	$\pm_{6.5}^{11.2}$	± 14.9	$\pm_{12.4}^{9.9}$	0.1253	$\pm_{18.1}^{7.6}$
60.0	1.3×10^{-3}	0.3952	$\pm_{1.5}^{2.8}$	± 11.3	$\pm_{8.3}^{8.2}$	0.3606	$\pm_{15.1}^{10.5}$
60.0	3.2×10^{-3}	0.3040	$\pm_{1.3}^{3.4}$	± 9.5	$\pm_{8.0}^{7.8}$	0.2957	$\pm_{16.4}^{9.5}$
60.0	5.0×10^{-3}	0.1860	$\pm_{2.6}^{3.5}$	± 13.2	$\pm_{8.0}^{7.9}$	0.1778	$\pm_{19.2}^{9.3}$
60.0	8.0×10^{-3}	0.1417	$\pm_{1.4}^{5.5}$	± 17.9	$\pm_{7.9}^{8.0}$	0.1457	$\pm_{19.4}^{6.9}$
60.0	2.0×10^{-2}	0.0519	$\pm_{6.8}^{10.9}$	± 56.4	$\pm_{13.4}^{9.9}$	0.0834	$\pm_{19.9}^{3.4}$

ulation HVQDIS. Also at higher $Q^2 > 100 \text{ GeV}^2$ the ZM-VFNS prediction fails to describe the D^* production [15].

In order to facilitate the comparison with previous measurements the cross sections are also measured in a reduced phase space of the D^* meson: $p_T(D^*) > 1.5 \text{ GeV}$ and $|\eta(D^*)| < 1.5$. They are listed in Tables 9 and 10. In Fig. 14 these measurements are shown as a function of Q^2 together with the results of the measurement at high Q^2 [15]. These measurements span over almost three orders of magnitude in Q^2 . The data are well described by CASCADE and the HVQDIS predictions with both PDF sets in the whole Q^2 range, while RAPGAP overshoots the data at high Q^2 .

7 Charm contribution to the proton structure function

The charm contribution $F_2^{c\bar{c}}(x, Q^2)$ to the proton structure function $F_2(x, Q^2)$ is related to the charm cross section in

the one photon exchange approximation by:

$$\frac{d^2\sigma^{c\bar{c}}}{dx dQ^2} = \frac{2\pi\alpha_{em}^2}{Q^4x} ([1 + (1 - y)^2] F_2^{c\bar{c}}(x, Q^2) - y^2 F_L^{c\bar{c}}(x, Q^2)). \tag{4}$$

Weak interaction effects are neglected and α_{em} denotes the electromagnetic coupling constant. The contribution from the structure function $F_L^{c\bar{c}}$ is less than 4% in the present $x - Q^2$ range. Assuming the ratio $F_L^{c\bar{c}}/F_2^{c\bar{c}}$ is predicted correctly within a model, the measured inclusive $D^{*\pm}$ cross sections $\sigma_{\text{vis}}^{\text{exp}}(y, Q^2)$ in bins of y and Q^2 are converted to a bin centre corrected $F_2^{c\bar{c}\text{exp}}(\langle x \rangle, \langle Q^2 \rangle)$ using the relation $Q^2 = xys$ and extrapolating σ_{vis} to the full phase space:

$$F_2^{c\bar{c}\text{exp}}(\langle x \rangle, \langle Q^2 \rangle) = \frac{\sigma_{\text{vis}}^{\text{exp}}(y, Q^2)}{\sigma_{\text{vis}}^{\text{theo}}(y, Q^2)} \cdot F_2^{c\bar{c}\text{theo}}(\langle x \rangle, \langle Q^2 \rangle). \tag{5}$$

Here $\sigma_{\text{vis}}^{\text{theo}}$ and $F_2^{c\bar{c}\text{theo}}$ are the theoretical predictions. The HVQDIS program is used to calculate $\sigma_{\text{vis}}^{\text{theo}}$ and $F_2^{c\bar{c}\text{theo}}$ in the NLO DGLAP scheme. In the kinematic range of the current analysis the beauty contribution to the D^* cross section is small. It is estimated with HVQDIS and subtracted for the determination of $F_2^{c\bar{c}}$.

The measurement covers about 50% of the total phase space for charm production. The extrapolation factor to the full phase space is model dependent. Since CASCADE also provides a reasonable description of the cross sections in the phase space covered in this analysis, it is used as an alternative model to determine $F_2^{c\bar{c}\text{exp}}$ in order to investigate this model dependence. The extrapolation factors in the present analysis, defined as the ratio of the full cross section $\sigma_{\text{full}}^{\text{theo}}$ to the cross section $\sigma_{\text{vis}}^{\text{theo}}$ in the visible phase space of the D^* meson, determined with HVQDIS and CASCADE, are compared in Fig. 15. They differ by about 10% at medium x . In the largest x bin the extrapolation factor as well as the difference between the two models increases significantly. In general the extrapolation factor determined with HVQDIS has smaller uncertainties than the one from CASCADE. Due to the larger phase space of the D^* meson in the present analysis compared to previous measurements, where the phase space coverage amounted to about 30%, the extrapolation factor to the full phase space is considerably smaller, although the model dependence of the extrapolation remains sizable.

In Table 11 and Fig. 16 the resulting $F_2^{c\bar{c}}$ extracted from the inclusive $D^{*\pm}$ cross sections with HVQDIS is shown as a function of x for different values of Q^2 . In addition to the experimental systematic uncertainties described in Sect. 6 the extrapolation (5) leads to an uncertainty. This extrapolation uncertainty is determined by varying the theory parameters listed in Table 2 simultaneously in the calculation of $\sigma_{\text{vis}}^{\text{theo}}$ and $F_2^{c\bar{c}\text{theo}}$. The resulting uncertainties on $F_2^{c\bar{c}}$ are shown separately in Fig. 16. HVQDIS and CASCADE both give a reasonable description of the measured cross sections and can be used to extract $F_2^{c\bar{c}}$. The differences obtained in $F_2^{c\bar{c}\text{exp}}$ for the two models are used to define the model uncertainty on $F_2^{c\bar{c}}$, which is also given in Fig. 16.

The results of a $F_2^{c\bar{c}}$ measurement based on lifetime information determined with the H1 silicon vertex detector CST [14] is compared to the present measurement in Fig. 16. The two measurements are based on independent methods with similar precision and agree very well. The $F_2^{c\bar{c}}$ determined with D^* mesons covers a larger range in x due to the larger η coverage of the CJs compared to the CST. It also has smaller uncertainties at low Q^2 , where the uncertainty of the lifetime based measurement is dominated by the light quark background.

Figure 16 also compares the FFNS NLO calculation of $F_2^{c\bar{c}}$ to the measurement using the MSTW2008f3 and CT10f3 proton PDFs. Both calculations give a reasonable

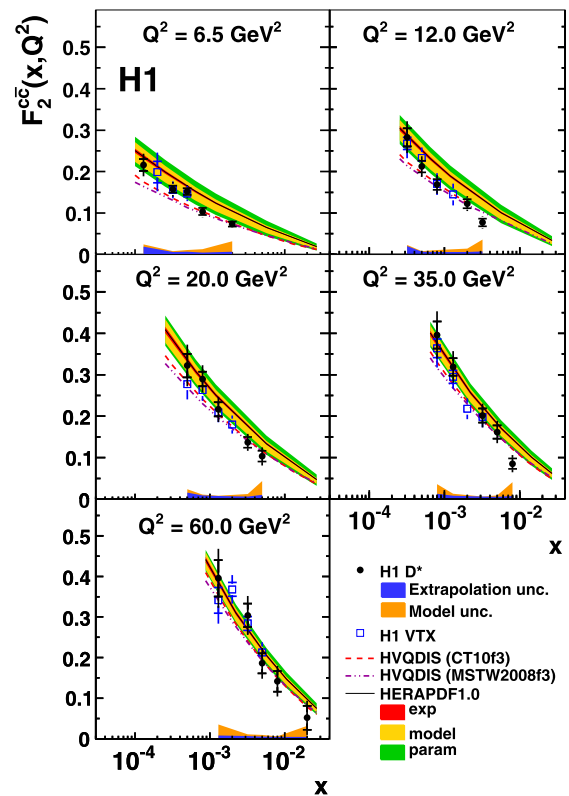


Fig. 16 $F_2^{c\bar{c}}$ as derived from D^* data with HVQDIS (points). The inner error bars show the statistical uncertainty, the outer error bar the statistical and experimental systematic uncertainty added in quadrature. The extrapolation uncertainty within the HVQDIS model is shown as blue band in the bottom of the plots. The outer (orange) band shows the model uncertainty obtained from the difference in $F_2^{c\bar{c}}$ determined with HVQDIS and CASCADE. The data are compared to the measurement of $F_2^{c\bar{c}}$ with the H1 vertex detector [14] (open squares), to NLO DGLAP predictions from HVQDIS with two different proton PDFs, and to the $F_2^{c\bar{c}}$ prediction of HERAPDF1.0

description of the data. The $F_2^{c\bar{c}}$ measurement is also compared to the $F_2^{c\bar{c}}$ prediction for HERAPDF1.0 [81], which has been extracted from the H1 and ZEUS combined inclusive proton structure function data. A general-mass variable-flavour-number scheme [82, 83] has been used which interpolates between the FFNS and the ZM-VFNS. The uncertainty on $F_2^{c\bar{c}}$ for the HERAPDF1.0 prediction is dominated by the variation of the charm mass in the PDF fit, which is included in the model uncertainty of the prediction. In general the prediction agrees with the $F_2^{c\bar{c}}$ measurement, showing that the gluon density determined from the scaling violations of the inclusive DIS cross section is consistent with that observed in charm production. At large x the central value of the HERAPDF1.0 prediction has a tendency to lie above the $F_2^{c\bar{c}}$ data, which may indicate a preference for a larger charm mass than the central value used for HERAPDF1.0, $m_c = 1.4$ GeV.

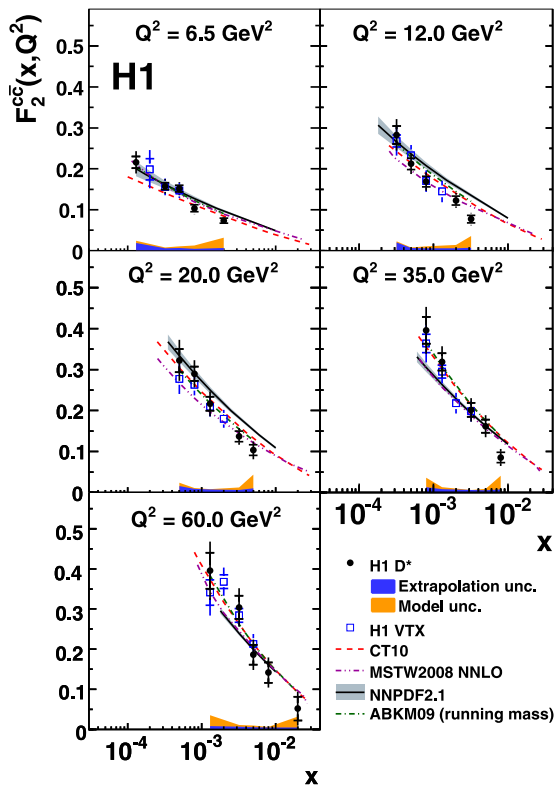


Fig. 17 $F_2^{c\bar{c}}$ as derived from D^* data with HVQDIS (points). The inner error bars show the statistical uncertainty, the outer error bar the statistical and experimental systematic uncertainty added in quadrature. The extrapolation uncertainty within the HVQDIS model is shown as blue band in the bottom of the plots. The outer (orange) band shows the model uncertainty obtained from the difference in $F_2^{c\bar{c}}$ determined with HVQDIS and CASCADE. The data are compared to the measurement of $F_2^{c\bar{c}}$ with the H1 vertex detector [14] (open squares) and to predictions from the global PDF fits CT10 (dashed line), MSTW08 at NNLO (dark dashed-dotted line), NNPDF2.1 (shaded band) and ABKM (light dashed-dotted line)

The $F_2^{c\bar{c}}$ measurement is compared to predictions from global PDF fits in Fig. 17: CT10 [47], MSTW2008 NNLO [84] and NNPDF2.1 [85] have been derived in general-mass variable-flavour-number schemes, while for the ABKM fit [86] the FFNS including higher order radiative corrections in QCD adopting the running \overline{MS} mass has been used. All predictions give a reasonable description of the measurement. At low Q^2 all predictions have a tendency to decrease less steeply with x than the data.

The measured $F_2^{c\bar{c}}$ as a function of Q^2 for different values of x is shown in Fig. 18. Scaling violations are observed. The Q^2 dependence of the data is well reproduced by the FFNS NLO calculation, but at low x the predictions are below the data, an effect which is larger if the MSTW2008f3 set is used as proton PDF. The HERAPDF1.0 prediction is in agreement with the data.

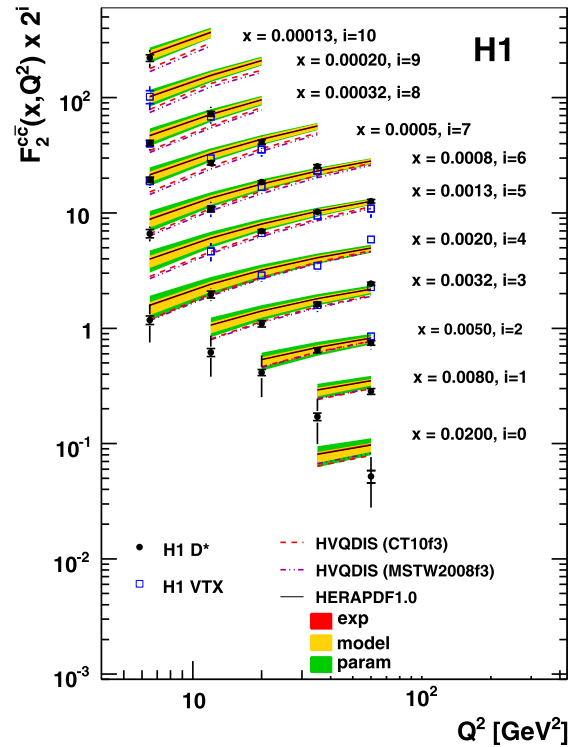


Fig. 18 $F_2^{c\bar{c}}$ as a function of Q^2 for different x , as derived from D^* data with HVQDIS (points). The inner error bars show the statistical uncertainty, the outer error bar the total uncertainty, including statistical, experimental systematic, extrapolation and model uncertainty added in quadrature. The data are compared to the measurement of $F_2^{c\bar{c}}$ with the H1 vertex detector [14] (open squares), to NLO DGLAP predictions from HVQDIS with two different proton PDFs, and to the $F_2^{c\bar{c}}$ prediction of HERAPDF1.0

8 Conclusion

A measurement of D^* meson production in deep-inelastic scattering is performed with a tenfold increase in statistics and a significantly enlarged phase space compared to the previous H1 measurement. Single and double differential cross sections are determined as a function of variables describing the kinematics of the event as well as of the D^* meson. The measurements are found to be reasonably well described by predictions based on the fixed-flavour-number scheme, namely the leading order Monte Carlo simulations RAPGAP and CASCADE as well as the next-to-leading order calculation HVQDIS. The data are also compared to a next-to-leading order calculation in the zero-mass variable-flavour-number scheme, which in general describes the data less well and is particularly high at low y .

The double differential cross section as a function of Q^2 and y is used to determine the charm contribution $F_2^{c\bar{c}}$ to the proton structure function F_2 . The extrapolation to the full phase space is done with two different models, using the next-to-leading order calculation HVQDIS and the Monte Carlo program CASCADE based on leading order matrix

elements and parton showers. The results for $F_2^{c\bar{c}}$ in these two models are very similar except for the highest x values. The results agree well with a measurement based on lifetime information determined with the H1 vertex detector. The data are well described by next-to-leading order calculations using different PDFs, showing that the gluon density determined from the scaling violations of the inclusive DIS cross sections is consistent with the one observed in charm production.

Acknowledgements We are grateful to the HERA machine group whose outstanding efforts have made this experiment possible. We thank the engineers and technicians for their work in constructing and maintaining the H1 detector, our funding agencies for financial support, the DESY technical staff for continual assistance and the DESY directorate for support and for the hospitality which they extend to the non-DESY members of the collaboration.

Open Access This article is distributed under the terms of the Creative Commons Attribution Noncommercial License which permits any noncommercial use, distribution, and reproduction in any medium, provided the original author(s) and source are credited.

References

- C. Adloff et al. (H1 Collaboration), *Z. Phys. C* **72**, 593 (1996). [arXiv:hep-ex/9607012](#)
- J. Breitweg et al. (ZEUS Collaboration), *Phys. Lett. B* **407**, 402 (1997). [arXiv:hep-ex/9706009](#)
- C. Adloff et al. (H1 Collaboration), *Nucl. Phys. B* **545**, 21 (1999). [arXiv:hep-ex/9812023](#)
- J. Breitweg et al. (ZEUS Collaboration), *Eur. Phys. J. C* **12**, 35 (2000). [arXiv:hep-ex/9908012](#)
- C. Adloff et al. (H1 Collaboration), *Phys. Lett. B* **528**, 199 (2002). [arXiv:hep-ex/0108039](#)
- S. Chekanov et al. (ZEUS Collaboration), *Phys. Rev. D* **69**, 012004 (2004). [arXiv:hep-ex/0308068](#)
- A. Aktas et al. (H1 Collaboration), *Eur. Phys. J. C* **38**, 447 (2005). [arXiv:hep-ex/0408149](#)
- A. Aktas et al. (H1 Collaboration), *Eur. Phys. J. C* **40**, 349 (2005). [arXiv:hep-ex/0411046](#)
- A. Aktas et al. (H1 Collaboration), *Eur. Phys. J. C* **45**, 23 (2006). [arXiv:hep-ex/0507081](#)
- A. Aktas et al. (H1 Collaboration), *Eur. Phys. J. C* **51**, 271 (2007). [arXiv:hep-ex/0701023](#)
- S. Chekanov et al. (ZEUS Collaboration), *J. High Energy Phys.* **0707**, 074 (2007). [arXiv:0704.3562](#)
- S. Chekanov et al. (ZEUS Collaboration), *Eur. Phys. J. C* **63**, 171 (2009). [arXiv:0812.3775](#)
- S. Chekanov et al. (ZEUS Collaboration), *Eur. Phys. J. C* **65**, 65 (2010). [arXiv:0904.3487](#)
- F.D. Aaron et al. (H1 Collaboration), *Eur. Phys. J. C* **65**, 89 (2010). [arXiv:0907.2643](#)
- F.D. Aaron et al. (H1 Collaboration), *Phys. Lett. B* **686**, 91 (2010). [arXiv:0911.3989](#)
- H. Abramowicz et al. (ZEUS Collaboration), *J. High Energy Phys.* **1011**, 009 (2010). [arXiv:1007.1945](#)
- F.D. Aaron et al. (H1 Collaboration), *Eur. Phys. J. C* **71**, 1509 (2011). [arXiv:1008.1731](#)
- R. Brun et al., GEANT3, Technical Report CERN-DD/EE-81-1 (1987)
- H. Jung, RAPGAP V3.1. *Comput. Phys. Commun.* **86**, 147 (1995)
- M. Bengtsson, T. Sjostrand, *Z. Phys. C* **37**, 465 (1988)
- V.N. Gribov, L.N. Lipatov, *Sov. J. Nucl. Phys.* **15**, 675 (1972). [*Yad. Fiz.* **15**, 1218 (1972)]
- V.N. Gribov, L.N. Lipatov, *Sov. J. Nucl. Phys.* **15**, 438 (1972). [*Yad. Fiz.* **15**, 781 (1972)]
- L.N. Lipatov, *Sov. J. Nucl. Phys.* **20**, 94 (1975). [*Yad. Fiz.* **20**, 181 (1974)]
- Y.L. Dokshitzer, *Sov. Phys. JETP* **46**, 641 (1977). [*Zh. Eksp. Teor. Fiz.* **73**, 1216 (1977)]
- G. Altarelli, G. Parisi, *Nucl. Phys. B* **126**, 298 (1977)
- T. Sjöstrand et al., PYTHIA V6.1. *Comput. Phys. Commun.* **135**, 238 (2001)
- B. Andersson, G. Gustafson, B. Soderberg, *Z. Phys. C* **20**, 317 (1983)
- B. Andersson, G. Gustafson, G. Ingelman, T. Sjostrand, *Phys. Rep.* **97**, 31 (1983)
- M.G. Bowler, *Z. Phys. C* **11**, 169 (1981)
- V. Kartvelishvili, A. Likhoded, V. Petrov, *Phys. Lett. B* **78**, 615 (1978)
- F.D. Aaron et al. (H1 Collaboration), *Eur. Phys. J. C* **59**, 589 (2009). [arXiv:0808.1003](#)
- A. Kwiatkowski, H. Spiesberger, H.J. Mohring, HERACLES V4.6. *Comput. Phys. Commun.* **69**, 155 (1992)
- P.M. Nadolsky et al., *Phys. Rev. D* **78**, 013004 (2008). [arXiv:0802.0007](#)
- J. Pumplin et al., *J. High Energy Phys.* **0207**, 012 (2002). [arXiv:hep-ph/0201195](#)
- H. Jung, CASCADE V2.0. *Comput. Phys. Commun.* **143**, 100 (2002)
- M. Ciafaloni, *Nucl. Phys. B* **296**, 49 (1988)
- S. Catani, F. Fiorani, G. Marchesini, *Phys. Lett. B* **234**, 339 (1990)
- S. Catani, F. Fiorani, G. Marchesini, *Nucl. Phys. B* **336**, 18 (1990)
- G. Marchesini, *Nucl. Phys. B* **445**, 49 (1995). [arXiv:hep-ph/9412327](#)
- H. Jung, [arXiv:hep-ph/0411287](#)
- E. Laenen, S. Riemersma, J. Smith, W.L. van Neerven, *Phys. Lett. B* **291**, 325 (1992)
- E. Laenen, S. Riemersma, J. Smith, W.L. van Neerven, *Nucl. Phys. B* **392**, 162 (1993)
- E. Laenen, S. Riemersma, J. Smith, W.L. van Neerven, *Nucl. Phys. B* **392**, 229 (1993)
- S. Riemersma, J. Smith, W.L. van Neerven, *Phys. Lett. B* **347**, 143 (1995). [arXiv:hep-ph/9411431](#)
- B.W. Harris, J. Smith, *Nucl. Phys. B* **452**, 109 (1995). [arXiv:hep-ph/9503484](#)
- B.W. Harris, J. Smith, *Phys. Rev. D* **57**, 2806 (1998). [arXiv:hep-ph/9706334](#)
- H.L. Lai et al. (CTEQ Collaboration), *Phys. Rev. D* **82**, 074024 (2010). [arXiv:1007.2241](#)
- A.D. Martin, W.J. Stirling, R.S. Thorne, G. Watt, *Eur. Phys. J. C* **70**, 51 (2010). [arXiv:1007.2624](#)
- L. Gladilin, [arXiv:hep-ex/9912064](#)
- G. Heinrich, B.A. Kniehl, *Phys. Rev. D* **70**, 094035 (2004). [arXiv:hep-ph/0409303](#)
- C. Sandoval, in *Proc. of XVII International Workshop on Deep-Inelastic Scattering*, DIS 2009, Madrid (2009). [arXiv:0908.0824](#)
- C. Sandoval, Inclusive production of hadrons in neutral and charged current deep inelastic scattering. Ph.D. Thesis, Univ. Hamburg (2009), DESY-THESIS-2009-044
- T. Kneesch, B.A. Kniehl, G. Kramer, I. Schienbein, *Nucl. Phys. B* **799**, 34 (2008). [arXiv:0712.0481](#)
- I. Abt et al. (H1 Collaboration), *Nucl. Instrum. Methods A* **386**, 310 (1997)
- I. Abt et al. (H1 Collaboration), *Nucl. Instrum. Methods A* **386**, 348 (1997)

56. R.-D. Appuhn et al. (H1 SpaCal Group), Nucl. Instrum. Methods A **386**, 397 (1997)
57. D. Pitzl et al., Nucl. Instrum. Methods A **454**, 334 (2000). [arXiv:hep-ex/0002044](#)
58. B. List, Nucl. Instrum. Methods A **501**, 49 (2001)
59. J. Becker et al., Nucl. Instrum. Methods A **586**, 190 (2008). [arXiv:physics/0701002](#)
60. C. Kleinwort, H1 alignment experience, in *Proceedings of the First LHC Detector Alignment Workshop*, ed. by S. Blusk et al. (2006), p. 41. CERN-2007-004
61. Th. Wolff et al., Nucl. Instrum. Methods A **323**, 537 (1992)
62. A. Baird et al., IEEE Trans. Nucl. Sci. **48**, 1276 (2001). [arXiv:hep-ex/0104010](#)
63. D. Meer et al., IEEE Trans. Nucl. Sci. **49**, 357 (2002). [arXiv:hep-ex/0107010](#)
64. B. Andrieu et al. (H1 Calorimeter Group), Nucl. Instrum. Methods A **344**, 492 (1994)
65. B. Andrieu et al. (H1 Calorimeter Group), Nucl. Instrum. Methods A **350**, 57 (1994)
66. T. Nicholls et al. (H1 SpaCal Group), Nucl. Instrum. Methods A **374**, 149 (1996)
67. M. Peez, Search for deviations from the Standard Model in high transverse energy processes at the electron-proton collider HERA. Ph.D. thesis, Univ. Lyon (2003), DESY-THESIS-2003-023 (available at http://www-h1.desy.de/publications/theses_list.html)
68. S. Hellwig, Untersuchung der $D^* - \pi_{\text{slow}}$ double tagging methode in charmanalysen. Dipl. thesis, Univ. Hamburg (2004) (available at http://www-h1.desy.de/publications/theses_list.html)
69. U. Bassler, G. Bernardi, Nucl. Instrum. Methods A **361**, 197 (1995). [arXiv:hep-ex/9412004](#)
70. K. Nakamura et al. (Particle Data Group), J. Phys. G **37**, 075021 (2010)
71. A.W. Jung, Measurement of the $D^{*\pm}$ meson cross section and extraction of the charm contribution, $F_2^c(x, Q^2)$, to the proton structure in deep inelastic ep scattering with the h1 detector at HERA. Ph.D. thesis, Univ. Heidelberg (2009), HD-KIP-09-01, DESY-THESIS-2009-001 (available at http://www-h1.desy.de/publications/theses_list.html)
72. G.J. Feldman et al., Phys. Rev. Lett. **38**, 1313 (1977)
73. J.E. Gaiser, Charmonium spectroscopy from radiative decays of the J/ψ and ψ' . Ph.D. thesis, Stanford University (1982)
74. P. Granet et al. (French-Soviet Collaboration), Nucl. Phys. B **140**, 389 (1978)
75. R.J. Barlow, Nucl. Instrum. Methods A **297**, 496 (1990)
76. W. Verkerke, D. Kirkby, The RooFit toolkit for data modeling. User Manual (2006). Available at <http://roofit.sourceforge.net>
77. D.L. Phillips, J. Assoc. Comput. Mach. **9**, 84 (1962)
78. A.N. Tikhonov, Sov. Math. Dokl. **4**, 1035 (1963). [Dokl. Akad. Nauk. SSSR **151**, 501 (1963)]
79. V. Blobel, in *Proc. Advanced Statistical Techniques in Particle Physics*, Durham (2002)
80. R. Brun, F. Rademakers, Nucl. Instrum. Methods A **389**, 81 (1997). ROOT version 5.18 with TUnfold version 14, the latter available at <http://www.desy.de/~sschmitt/tunfoldd.html>
81. F.D. Aaron et al. (H1 and ZEUS Collaboration), J. High Energy Phys. **1001**, 109 (2010). [arXiv:0911.0884](#)
82. R.S. Thorne, R.G. Roberts, Phys. Rev. D **57**, 6871 (1998). [arXiv:hep-ph/9709442](#)
83. R.S. Thorne, Phys. Rev. D **73**, 054019 (2006). [arXiv:hep-ph/0601245](#)
84. A.D. Martin, W.J. Stirling, R.S. Thorne, G. Watt, Eur. Phys. J. C **63**, 189 (2009). [arXiv:0901.0002](#)
85. R.D. Ball et al., Nucl. Phys. B **849**, 296 (2011). [arXiv:1101.1300](#)
86. S. Alekhin, S. Moch, Phys. Lett. B **699**, 345 (2011). [arXiv:1011.5790](#)